PhD Dissertation 2007

Integration of Nanomechanical Sensors on CMOS by Nanopatterning Methods

Julien Arcamone

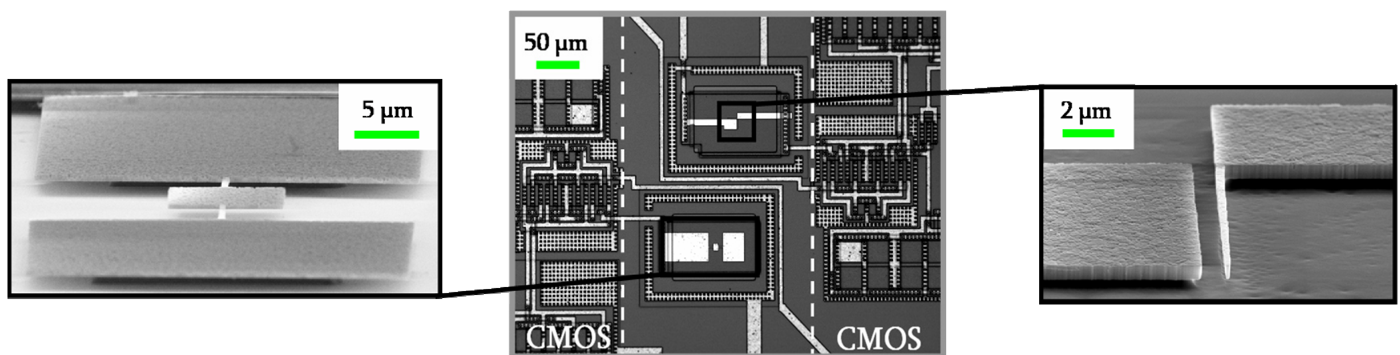

CNM Centre Nacional de Microelectrònica IMB

UAB Universitat Autònoma de Barcelona

INSA LYON

INL

Directors:
Dr. Francesc Pérez-Murano (CNM-IMB CSIC)
Pr. Georges Brémond (INSA Lyon, INL-CNRS)

Tutor UAB:
Pr. Francesc Serra Mestres

El doctor Francesc Pérez-Murano, Investigador Científic del Consell Superior d'Investigacions Científiques (CSIC) a l'Institut de Microelectrònica de Barcelona (CNM-IMB),
i el doctor Georges Brémond, Professor al INSA de Lyon i investigador del Centre Nacional d'Investigacions Científiques (CNRS) a l'Institut de Nanotecnologia de Lyon,

CERTIFIQUEN

que la present memòria titulada 'Integration of nanomechanical sensors on CMOS by nanopatterning methods' ha estat realitzada sota la seva direcció per en Julien Arcamone

Bellaterra y Villeurbanne, juliol 2007

à Charlotte, Gamin, Nelly et Jean

ACKNOWLEDGEMENTS

Without the help and the intellectual, psychological and material support of many people, I could not have done this work. Therefore, I want to thank very gratefully everyone who has indirectly or directly participated to it.

I would like to thank very sincerely my two co-directors, Dr Francesc Pérez-Murano and Pr Georges Brémond, for their respective contribution.

I am also very grateful to all the other members of my committee who make me the honor to attend my PhD defense: Dra Arantxa Uranga, Pr Emilio Lora-Tamayo, Dr Hans Loeschner and Dr Liviu Nicu.

Querría agradecer ante todo a Francesc Pérez-Murano por haber dirigido 'intensamente' mi tesis y haberme animado continuamente. A nivel profesional, me ha transmitido mucho de su saber, en particular su capacidad de analizar los hechos con perspectiva y síntesis. Gracias por todo.

Quiero agradecer también al director del CNM, el profesor Francesc Serra Mestres, por haberme ofrecido la posibilidad de trabajar en su centro. Quiero dar todo mi sincero reconocimiento a los que han colaborado estrechamente conmigo: Ana Sánchez-Amores, Gemma Rius, Marta Duch, Marta Gerboles, Joseph Montserrat, Raquel Palencia, Josep Lorente, Guillermo Villanueva, Alberto Moreno y todos los otros, perdonadme por olvidarme. Sin la ayuda, el apoyo y los consejos de Bertrand Mishischi, el diseño del circuito hubiera sido imposible, muchísimas gracias a Paco Serra-Graells por su ayuda fundamental y su disponibilidad.

Muchas gracias también a todos los sucesivos miembros del despacho por los buenos momentos pasados: Gemma, Cristina, Olga, Guillermo, Andreu, Nadia, Iñigo, Irene, Giulio, Servane, Marc… Un saludo a todos los otros: Neus, Roger, Olivier, Pierre, Marcel, Nico, Roger, Jofre…

Querría dar un saludo especial y agradecer a los miembros del laboratorio ECAS de la ETSE-UAB: Pra Nuria Barniol, Dr Gabriel Abadal, Dra Arantxa Uranga, Dr Francesc Torres y Jordi Teva. Un saludo especial también a Mari-Carmen Mesas.

De l'INSA Lyon et l'INL, je voudrais chaleureusement remercier mon second directeur de thèse, le Pr. Georges Brémond, pour son soutien et son aide notamment lors de mes passages à Lyon. J'ai une pensée particulière pour Pavel Budau qui nous a aidés avec enthousiasme et qui nous a quittés entre-temps dans des circonstances malheureuses. Merci aussi à Philippe Girard pour sa contribution à ce travail. Enfin, je tiens à remercier particulièrement le professeur Gérard Guillot de m'avoir accueilli au sein de l'INL, anciennement le LPM.

I will not forget my colleagues of EPFL: Dr Lianne Doeswijk and of course Pr Jürgen Brugger and Dr Marc van den Boogaart with whom we have been carrying out a very fruitful collaboration and with whom I also have spent friendly times.

Un grand merci aussi aux Dr Thierry Ondarçuhu et Erik Dujardin pour leur accueil lors de ma venue au CEMES-CNRS de Toulouse lors de notre fructueuse collaboration.

Je terminerai par mes proches. Charlotte, tu m'as supporté et encouragé constamment durant ces périodes intenses d'écriture: je ne sais comment te remercier pour ce que tu as fait pour moi. Je veux enfin exprimer toute ma gratitude envers mes parents pour tout leur soutien et tout ce qu'ils ont aussi fait pour moi jusqu'au jour d'aujourd'hui: c'est un peu pour vous que j'ai écrit ce manuscrit. Merci à toi aussi Benjamin pour ta fraternité, ainsi qu'à Manine et tous les autres que je n'oublie pas.

INDEX

THESIS PRESENTATION PAGE 1

CHAPTER 1. INTRODUCTION TO NANO/MICROMECHANICAL RESONATORS AND SYSTEMS PAGE 5

I. General Introduction 5
I.1. MEMS overview 7
I.2. NEMS: interest and features 9
II. Nanopatterning techniques overview 11
III. Nano/micromechanical resonators. Interest and physical features 14
III.1. Types of nano/micromechanical resonators 14
III.2. Mechanisms determining the quality factor and the noise 15
III.3. Characterization techniques of frequency response 17
IV. NEMS-based mass sensors 19
IV.1. Quartz-crystal microbalances: applications and performance 19
IV.2. State-of-the-art of mass sensors based on micro/nanomechanical resonators 19
Bibliographical references 22

CHAPTER 2. CONCEPTS OF NANO/MICROMECHANICAL RESONATORS FOR MASS SENSING APPLICATIONS WITH ALL ELECTRIC ACTUATION AND DETECTION PAGE 31

I. Response of micro/nanomechanical resonators-based systems 34
I.1. Equations of oscillating systems 34
I.1.a. Harmonic (undamped non-driven) oscillators 34
I.1.b. Damped non-driven oscillators. 35
I.1.c. Driven damped oscillators 35
I.2. Resonance frequency of nano/micromechanical resonators: Analytical modeling 37
I.2.a. General equations 37
I.2.b. Cantilever and bridge 40
I.2.b.i) Cantilever 40
I.2.b.ii) Bridge 42
I.2.c. Quad-beams resonators 42
I.3. Mass sensitivity of nano/micromechanical resonators 48
I.3.a. Calculation of mass sensitivity 48
I.3.a.i) Punctual mass sensitivity 48
I.3.a.ii) Areal mass sensitivity 49
I.3.b. Dynamic linear range 50
II. Electrical response of electrostatically driven resonators 51
II.1. Transduction principle: capacitive detection with electrostatic actuation 51
II.2. Equivalent electrical modeling of a mechanical resonator 52
II.2.a. Global equivalent electrical scheme 52
II.2.b. RLC equivalent model of the motional impedance 54
II.2.b.i) Phenomenological approach of a RLC oscillator 54
II.2.b.ii) Parameters calculation 57
II.2.c. Global response 59
II.3. Response to electrostatic actuation 60
II.3.a. Deflection and pull-in voltage related to electrostatic force 60
II.3.b. Spring-softening effect 62
II.3.c. Generalization 63
III. Two approaches of flexural mode resonators: Out-of-plane and in-plane vibrating resonators 65
III.1. Out-of-plane flexion mode resonators 65
III.1.a. Comparison in terms of electrical response of three discrete devices with simplified RLC model 65
III.1.b. Comparison in terms of mass sensitivity (punctual and distributed) 67
III.1.b.i) Punctual mass sensitivity 67
III.1.b.ii) Distributed mass sensitivity 67
III.1.c. Analysis of the quad-beams device 68
III.1.c.i) Electromechanical modeling 68
III.1.c.ii) Fabrication of discrete devices: e-beam lithography on SOI 70
III.1.c.iii) Measurement of discrete devices 72
III.2. In-plane flexion mode resonators. Cantilevers 74
Conclusion of chapter 2 76
Bibliographical references 77

CHAPTER 3. DEVICE MODELING AND IC DESIGN OF NANO/MICROMECHANICAL RESONATORS ON CMOS CIRCUITRY PAGE 81

I. Interest of monolithic integration with CMOS....83
I.1. Comparison integrated/discrete structures.... 83
I.2. State-of-the-art of circuit topologies 84
II. Integration of NEMS on CMOS....86
II.1. Design of CMOS integrated NEMS resonators.... 86
II.1.a. In-plane vibrating cantilevers.... 86
II.1.b. Out-of-plane vibrating QB.... 86
II.2. CCII CMOS circuit characteristics.... 87
II.2.a. CCII Circuit topology.... 87
II.2.b. CCII circuit performance 90
II.2.b.i) Determination of operation points (DC) 91
II.2.b.ii) AC response 92
II.2.b.iii) Transient simulations 95
II.2.b.iv) Conditions of saturation 97
II.2.b.v) Linearity of the circuit response 97
II.2.b.vi) Noise analysis 98
II.2.c. CCII circuit performance with NEMS model at input 99
II.2.c.i) Electrical simulations of cantilevers-CCII mixed circuit.... 99
II.2.c.ii) Electrical simulations of QB-CCII mixed circuit 105
II.3. NEMS/CMOS circuit layout.... 108
II.3.a. CCII Circuit layout, integration areas layout.... 108
II.3.b. Chip layout 111
Conclusion of chapter 3....113
Bibliographical references 114

CHAPTER 4. FABRICATION OF NANO/MICROMECHANICAL RESONATORS ON CMOS CIRCUITRY PAGE 117

I. Lithography techniques for integration of NEMS on CMOS 120
I.1. Nanostencil lithography, a full-wafer high-resolution technique 120
I.1.a. State of the art, features and advantages of the technique 120
I.1.b. Fundamental aspects of the fabrication of a full-wafer stencil by DUV.... 122
I.1.c. Specific nanostencil layout for CNM CMOS wafer 125
I.2. Electron beam lithography 127
II. Fabrication of micro/nanomechanical resonators on CMOS by nanostencil lithography (nSL).... 128
II.1. CNM CMOS technology 129
II.2. Optimization of nSL process on CMOS: alignment and blurring corrections.... 131
II.2.a. Alignment.... 131
II.2.b. Blurring of Al patterns deposited by nSL.... 133
II.2.c. Dummy wafers 139
II.3. Post-processing of pre-fabricated CMOS wafers based on nSL.... 141
II.3.a. *poly1* removal.... 141

II.3.b. Alignment ... 142
II.3.c. Al deposition ... 144
II.3.d. Blurring correction ... 145
II.3.e. Pattern transfer and release ... 145
II.3.f. Test of CMOS compatibility of nSL ... 148
III. Fabrication of nano/micromechanical resonators on CMOS by electron-beam lithography (eBL) 150
Conclusion of chapter 4 ... 151
Bibliographical references ... 152

CHAPTER 5. EXPERIMENTAL CHARACTERIZATION OF NEMS/CMOS DEVICES

PAGE 155

I. Experimental procedure and measurement set-up ... 156
II. CCII circuit characterization ... 158
III. Electrical measurements of the frequency response of integrated resonators ... 159
III.1. Electrical measurement of in-plane vibrating cantilevers ... 159
III.1.a. Samples characteristics ... 159
III.1.b. Experimental results ... 161
III.1.b.i) Measurements in air with set-up 1 ... 161
III.1.b.ii) Measurements in vacuum with set-up 2 ... 162
III.1.b.iii) Estimation of the Young modulus of the structural layer ... 163
III.1.b.iv) Electrical results summary ... 164
III.1.c. Analysis of results ... 165
III.1.c.i) Estimation of the fringing field parasitic capacitance C_{PA} ... 165
III.1.c.ii) Driving voltage effect: spring-softening ... 165
III.1.c.iii) Q factor evolution as a function of the pressure ... 167
III.1.c.iv) Estimation of critical deflection ... 168
III.1.c.v) Noise considerations ... 169
III.2. Electrical measurement of out-of-plane vibrating quad-beams ... 171
III.2.a. Samples characteristics ... 171
III.2.b. Experimental results ... 171
III.2.b.i) Measurements in air with set-up 1 ... 172
III.2.b.ii) Measurements in vacuum with set-up 2 ... 172
III.2.b.iii) Electrical Results Summary ... 173
III.2.c. Analysis of results ... 174
III.2.c.i) Estimation of the fringing field parasitic capacitance C_{PA} ... 174
III.2.c.ii) Q factor evolution as a function of the pressure ... 174
III.2.c.iii) Driving voltage effects ... 175
Conclusion of chapter 5 ... 177
Bibliographical references ... 178

CHAPTER 6. FUNCTIONAL CHARACTERIZATION. IMPLEMENTATION OF NEMS/CMOS AS MASS SENSORS PAGE 179

I. Punctual mass sensing ... 181
I.1. Monitoring the evaporation of femtoliter droplets (exp. I) ... 181
I.1.a. Experimental set-up ... 182
I.1.b. Results and analysis ... 186
I.2. Double cantilever resonators (exp. II) ... 189
I.2.a. Features of double cantilever devices ... 189
I.2.b. Results of mass sensing ... 195
II. Distributed mass sensing experiments ... 200
II.1. Monitoring the deposition of ultra-thin gold layers (exp. III) ... 202
II.1.a. Experimental set-up ... 202
II.1.b. Nanomechanical sensor ... 206
II.1.c. Results and analysis ... 207
II.2. Application of NEMS/CMOS mass sensors as positioning sensors (exp. IV) ... 216
II.2.a. Quasi-dynamic approach ... 216
II.2.b. System description ... 216
II.2.b.i) Alignment procedure ... 218
II.2.b.ii) Mass sensor requirements ... 220
Conclusion of chapter 6 ... 223
Bibliographical references ... 224

GENERAL CONCLUSION PAGE 227

ANNEX PAGE 231

A1. Resum en català ... 232
A2. Resumen en castellano ... 234
A3. Résumé en français ... 236
A4. Zusammenfassung auf Deutsch ... 238
A5. Glossary ... 239
A6. Complete diagram of the CCII CMOS circuit ... 240
A7. Technological processes ... 241
A7.1. CNM CMOS process ... 241
A7.2. Dummy wafers process ... 247
A7.3. Post-processing based on eBL ... 250
A7.4. Experimental results of pattern transfer of nanostencil lithography ... 251
A8. QSD system: schematic of the mechanical holder of the sensor ... 253
A9. AFM characterization of resonators: preliminary work ... 254
A10. List of publications ... 257

THESIS PRESENTATION

This PhD thesis has been mainly realized at the 'Centro Nacional de Microelectrónica' – 'Instituto de Microelectrónica de Barcelona' (CNM-IMB), that is part of the 'Consejo Superior de Investigaciones Científicas' (CSIC) (Spanish National Research Council), and directed there by Dr. Francesc Pérez-Murano. It has also been partly carried out at INSA Lyon, at the 'Institut de Nanotechnologie de Lyon' laboratory (INL), that is part of the 'Centre National de la Recherche Scientifique' (CNRS) (French National Research Center), and directed there by Pr. Georges Brémond.

This work must be placed in a context of rapid and growing expansion of the interest for the so-called 'nanotechnologies'. This denomination actually covers an extremely wide range of applications which are related to very different scientific disciplines, like physics, chemistry, microelectronics, biology and biochemistry, materials science in general, etc...

Besides other research topics, like nano-materials (that find applications from metallurgy to medicine), the field of nanosensors is also extremely attractive because ultra-miniaturized sensing devices feature very high sensitivities to many different signal domains, like pressure, temperature, mass, mechanical stress, chemical adsorption, etc... Within this field, the scope of this thesis is related to resonant nanomechanical devices applied as ultra-sensitive mass sensors. A smart nanosystem has been developed based on a monolithic integration of a mechanical resonating device with CMOS.

At the beginning, this work partially relied on the previous experience of CNM acquired during its participation to the NANOMASS[1] project in which a similar approach was followed except for two major differences: a different interfacing CMOS circuit for the readout of the resonance

[1] Project funded by the European Commission within the FP5 (5th Framework Program), contract nº IST-1999-14053

signal and alternative nanolithography methods to define the nanodevices have been employed. In the NANOMASS project, the functionality of first prototypes was demonstrated. However, in the present work, the fabrication process has been improved in order to drastically increase the yield and a much better functionality of the devices has been demonstrated.

The work of this thesis has been carried out in the frame of the NaPa[2] project, whose objective is to develop emerging nanopatterning techniques which could be transferred to industry in short/medium terms. A complementary objective has been to promote possible applications, i.e. innovative nanodevices, using those techniques. Hence, the main goals of this thesis have been the simultaneous developments of (i) CMOS integrated nano (and micro) electromechanical systems (N-MEMS), and of (ii) an entire N-MEMS processing technology based on an advanced nanolithography technique named 'nanostencil', in order to fabricate monolithic systems with high yield and throughput.

This thesis features three well-distinct aspects: (i) the design of a nanodevice, (ii) its fabrication using nanofabrication techniques and (iii) its operation for sensing applications.

Concretely, it has consisted first in modeling and designing nano/micromechanical resonators, then the advantages and the feasibility of a monolithic integration on CMOS have been studied. Indeed, CMOS-NEMS are attractive systems which combine unprecedented sensing (and actuating) attributes originated by the mechanical part with the possibility of detecting the sensing signal in enhanced conditions (reducing parasitic loads) through the on-chip circuitry that can complementarily amplify and condition it.

These devices have been subsequently fabricated at full-wafer scale combining a standard CMOS technology with emerging nanolithography techniques, in particular with nanostencil lithography (nSL) whose practical implementation and patterning resolution have been optimized through a collaboration with EPFL (École Polytechnique Fédérale de Lausanne, Switzerland) in the frame of the NaPa project.

Then, the successful operation of the system has been demonstrated by characterizing precisely the frequency response of the micro/nanomechanical structure whose output signal is obtained under the form of an alternate electrical signal detected and amplified through a new specifically designed CMOS readout circuitry. Finally, this CMOS-NEMS resonator has been implemented as an ultra-sensitive mass sensor in four distinct experiments oriented to either scientific or technical purposes.

This PhD dissertation is structured in six chapters. Chapter 1 introduces the field of MEMS and their further evolution towards NEMS. With regard to this matter, an overview of modern nanopatterning techniques is given. Then, a survey of existing nano/micromechanical resonators is presented in terms of specific attributes and physical features: a special focus is given on the specific application of these resonating nano/micromechanical resonant structures as ultra-sensitive mass sensors.

[2] "Emerging Nanopatterning methods" project funded by the European Commission within FP6 (6th Framework Program), 31 (academic and industrial) partners from 14 countries (contract NMP4-CT-2003-500120)

In chapter 2, three types of nano/micromechanical resonators are analytically modeled in order to predict their mechanical frequency response. With the aim of electrically actuating and detecting the nanodevices, a capacitive detection scheme is adopted and an electromechanical model is followed to calculate their electrical response when mechanically resonating.

With regard to this matter, a specific low-power CMOS readout circuit has been designed. Its specifications have been defined according to theoretical predictions of resonance signal levels. Chapter 3 describes its topology and its operation principle. Its intrinsic behavior as well as its behavior when coupled to the electromechanically modeled nano/micromechanical resonator are fully analyzed based on simulations results.

Nevertheless, the practical realization of such CMOS integrated devices is challenging. In terms of fabrication, a full-wafer cost-effective integration of NEMS on CMOS still had to be demonstrated at this time. Because of this, a collaboration with EPFL (École Polytechnique Fédérale de Lausanne) was undertaken to further develop nanostencil lithography with the aim of integrating at full-wafer scale mesoscopic (nano and micro) structures on pre-fabricated CMOS circuitry. Chapter 4 describes the main initial issues that were identified and then solved. The successfully developed post-processing technology leading to the full-wafer integration of NEMS on CMOS in one single nSL step will be entirely detailed. In parallel, a second approach based on electron beam lithography with the aim to fabricate rapidly new prototypes of nanodevices on CMOS is also presented.

The complete characterization in air and vacuum of the obtained CMOS-NEMS is detailed in chapter 5. The main features of the frequency response, the experimental signal levels and the effect of the driving voltage on the mechanical frequency response are discussed.

Finally, chapter 6 focuses on the implementation of these CMOS-NEMS as ultra-sensitive mass sensors. This is currently one of the most explored applications of NEMS since nano/micromechanical resonators offer outstanding advantages in terms of sensitivity and integration compared to widely used quartz-crystal microbalances (QCM). Due to their small size, NEMS resonators inherently offer high mass sensing attributes together with a spatial resolution.

Four different experiments that have been designed and carried out are described in this chapter: (i) monitoring the evaporation of droplets to analyze wetting mechanisms at the femtoliter scale, (ii) a novel device is presented and tested that allows making reliable mass measurements in ambient conditions by directly providing the measurement uncertainty, (iii) monitoring in-situ the deposition of ultra-thin gold layers (sub-monolayer coverage). (iv) the very high areal mass sensitivity featured by the CMOS-NEMS has led us to implement it as a positioning sensor in a quasi-dynamic stencil lithography system, that is presently under development jointly with EPFL.

At the end, an annex section provides additional information: summaries in Catalan, Spanish, French and German, as well as technical data and schematics. Finally, a list of publications related to this thesis is presented.

CHAPTER 1

INTRODUCTION TO NANO/MICROMECHANICAL RESONATORS AND SYSTEMS

I. General Introduction 5
I.1. MEMS overview 7
I.2. NEMS: interest and features 9
II. Nanopatterning techniques overview 11
III. Nano/micromechanical resonators. Interest and physical features 14
III.1. Types of nano/micromechanical resonators 14
III.2. Mechanisms determining the quality factor and the noise 15
III.3. Characterization techniques of frequency response 17
IV. NEMS-based mass sensors 19
IV.1. Quartz-crystal microbalances: applications and performance 19
IV.2. State-of-the-art of mass sensors based on micro/nanomechanical resonators 19
Bibliographical references 22

I. General Introduction

In the late 1970s, the semiconductor microelectronics industry gave rise to a new branch of science and technology referred to as microtechnology. Benefiting from the know-how in terms of materials and miniaturization processes acquired through the fabrication of silicon integrated circuits (IC), diverse types of mechanical devices with dimensions in the deep submillimeter range, typically 100 microns (μm) or below, could be fabricated from then on.

In fact, for more than one hundred years already, the watchmaking industry mastered the fabrication of miniature mechanical pieces but the more recent booming of microtechnology comes from the coincidence that the silicon material used in IC also has outstanding mechanical properties [1], in particular a high Young modulus (around 160 GPa) and a wide and very linear elastic range. In parallel, the possibility to manufacture it under crystalline or polycrystalline

forms results in low dissipation layers. Another advantage comes from the fact that its processing is very well known and cost effective.

The outstanding electrical and mechanical properties of silicon allow designing smart mixed electro-mechanical monolithic components which involve on one hand a silicon micromechanical element for sensing (or actuating) purposes, and on another a microelectronics complementary-metal-oxide-semiconductor (CMOS) circuitry to control it.

Applicable to a broad range of sensing and actuating purposes, devices known as microelectromechanical systems (MEMS) provide enhanced sensitivity and resolution owing basically to their reduced size. Physically, they also access new interesting mechanisms that cannot be observed at macroscopic scales.

MEMS fabrication technology offers the possibility of very large scale integration (VLSI) of ultra-compact devices in a batch fabrication process. For this reason, a growing number of companies are already selling different types of MEMS-based products for clients coming from the automotive industry (the most famous is the accelerometer used in car airbags) until the biomedical sector (electronic blood pressure equipment, for instance).

Throughout the 80s and the 90s, MEMS have progressively been scaled down but not as fast as the Moore's law that guides the constant diminution of transistors size in IC. The obtained advantages when scaling down a mechanical element in the micron range and below are maybe not as straightforward as when a transistor is scaled down whereby faster and more complex functions per unit space are yielded. There is also maybe a cost reason as the MEMS market is not yet as profitable as the IC market although it also requires heavy investments in research and development.

However, jointly with the birth of the so-called 'nanotechnology' in the late 90s and the advances provided by novel deep-submicron CMOS processes, MEMS technology has recently derived towards a further miniaturization, under the form of so-called 'nanoelectromechanical systems' (NEMS). Indeed, a reduction of dimensions towards nanometer scale does not only represent a further and natural improvement: this leads not only to extremely high sensitivities and very high natural resonance frequencies but also new physical effects can be explored by the fact of getting closer to the atomic scale.

This global trend has created new needs in terms of lithography, and new versatile techniques are now required to scale down devices and thereby to reach nanometer resolution. Definitely, a certain number of nanopatterning techniques are already available like deep-ultra-violet lithography (DUV), immersion lithography (IL) or electron-beam lithography (eBL). The first two techniques represent a huge investment cost only affordable for large microelectronics foundries but prohibited de facto to research laboratories interested in the design of nanodevices. On the contrary, the use of eBL has democratized in the last few years as its use has spread among research laboratories. Its inherent low throughput arising from the serial operation does not constitute a limitation for research purposes but it does for industrial applications. Cheaper, parallel and 'clean' (resistless if possible) nanopatterning techniques are nowadays highly needed.

With regard to these matters, a short review of existing MEMS is going to be presented. Then, some interesting and specific features of NEMS considering them as further evolution of MEMS will be described. To fabricate NEMS, modern nanopatterning techniques are required: they will be briefly introduced. Finally, a short survey of existing nano/micromechanical resonators will be exposed insisting on the application as ultra-sensitive mass sensors.

I.1. MEMS overview

Microelectromechanical devices (or systems, i.e. MEMS) are miniaturized structures that are mechanically stimulated by an input electromechanical transducer. The mechanical response under the form or static or dynamic motion is then translated back into an output electrical signal through another application-specific electromechanical transducer.

Very diverse actuation and detection schemes of the mechanical motion exist. Interestingly, the mechanical element, depending on its shape and mode of operation, can be applied to versatile sensing purposes. Pressure, temperature, angular rate and all types of chemical sensors as well as accelerometers, gas chromatographs and radio-frequency (RF) MEMS have been developed. In nature, MEMS science and technology are multi-disciplinary and require know-how in electronics and mechanical engineering as well as in material science, eventually in chemistry and theoretical physics.

The materials constituting MEMS, the mechanical part and its electrical connections, are generally the ones utilized in the microelectronics industry: silicon (single or- polycrystal), silicon compounds like silicon oxide (SiO_2), silicon nitride (Si_3N_4) and eventually silicon carbide (SiC), III-V materials like GaAs, and metals like copper or aluminum.

The interest of scaling down mechanical devices can be understood considering the transformation of very general magnitudes affected by a scaling factor K, defined as K=transformed dimension (miniaturized) / reference dimension (macro) (i.e. $K<1$). Table I - 1 illustrates the improvements resulting from a miniaturization through an emphasis on the mechanical resonance frequency and the mass sensitivity (proportional to m/f_0).

magnitude	scaling factor
length (L)	K
area (A)	K^2
volume (V), i.e. mass (m)	K^3
stiffness (k)	K
resonance frequency (f_0)	K^{-1}
mass sensitivity (S)	K^4
thermal time constant (τ)	K

Table I - 1. Scaling factor for several magnitudes

Decreasing the size of the device (i.e. K), higher resonance frequencies (scaled as K^{-1}) can be obtained what is interesting for high frequency applications (telecommunication devices, etc...) and in parallel, a drastic enhancement of the mass sensitivity (equivalent to the ratio m/f_0, the precise calculation is detailed later) is yielded (K^4 scale factor). The thermal time constant is also reduced what physically means that the dissipation of power may become an issue in small structures. This also has to see with the fact that the surface to volume ratio equal to K^{-1} is increased: surface-related effects like thermal losses will become increasingly important.

These specific examples give anyway general trends of the influence of the size reduction of mechanical devices. At smaller scales down to the micron range, the physics is still the same but the dominant effects are modified with respect to macroscopic scales.

Among all the existing types of MEMS, the main types are:

- pressure sensors. They generally rely on a bulk micromachined membrane of which one side is vacuum sealed. The deformation caused by the differential pressure between both sides is sensed using piezoresistors or capacitively.
- inertial sensors: accelerometers or gyroscopes. Such sensors are widely used for military and automotive applications. Generally, accelerometers are bulk micromachined and can be sensed either piezoresistively or capacitively. MEMS gyroscopes vibratory are so far exclusively vibratory [2]. They rely on the Coriolis force and are generally sensed capacitively.
- chemical sensors. For the monitoring of chemical reactions, very different approaches of chemical MEMS are reported: chemomechanics-based, thermal effects-based, integrated optics-based, or electrochemistry-based.
- RF MEMS. There exist four main types [3]: (i) switches, varactors and inductors operable from DC to 120 GHz in relatively mature technologies; (ii) micromachined transmission lines; (iii) thin film bulk acoustic resonators (FBAR) and filters that base on acoustic vibrations of thin films in the GHz range and with high quality factor (Q-factor, further defined) (>2000); (iv) RF micromechanical resonators and filters until 100 MHz. In general, they achieve high Q only in vacuum: this technology is not ready yet for commercial applications but represents a very promising way to form reference clock circuits.
- power related applications. In the last few years, these devices have faced an increasing interest. Fuel cells and microgenerators [4] are now two hot topics.
- scanning probes. The successful development in the mid-80s of scanning tunneling [5] and atomic force microscopy [6], constituting a breakthrough towards the further emergence of nanotechnology, partially relies on the development of the microfabrication techniques to make cantilever (singly clamped beams)-based scanning probes with sharp tip apex.

Since the early development of MEMS technology, researchers have been trying to co-integrate microelectromechanical devices with bipolar or CMOS on-chip circuitry to fabricate monolithic microsystems. Another opposite alternative is the heterogeneous integration of different types of components. Simple heterogeneous systems link the die wherein the sensing microdevices are located to a PCB containing IC chips by means of a wire bonding. Compacter solutions require an increasing complexity of the packaging process.

To make monolithic devices, a CMOS technology and micromachining (either bulk or surface) techniques have to be combined in order to fabricate smart microsystems that can be of all the previously cited types. These CMOS integrated sensors benefit from a reduction of parasitic loading due to the very short distance between the sensing and the circuit parts, thus allowing improving the signal over noise ratio (SNR) and drastically upscaling the number of parallel controllable sensors in a single chip. The CMOS circuitry offers convenient mixed-signal possibilities to collect, amplify and condition the raw electrical signal originated by the mechanical part of the MEMS: as an example of application the signal can be calibrated, compensated and linearized on-chip. In RF MEMS, monolithic implementations integrate a variety of high Q and low insertion loss components with RF transistors.

In terms of technology, three approaches exist: pre-, intra- and post-CMOS micromachining. In order not to interfere with reproducible and stable CMOS processes, the post-CMOS is mostly used owing to its flexibility. However, commonly to those three methods, the complexity of the combination between CMOS and micromachining processes, together with packaging issues have been a constant limitation to the achievement of fully integrated MEMS.

In this context, following a trend pulled by the development of modern deep submicron CMOS technologies, MEMS have further evolved towards the submicron scale, that is nanoscale, to constitute the new category of nanoelectromechanical systems (NEMS). In analogy with the new phenomena encountered in sub-50 nm MOS transistors related to quantum physics (like short channel effect), NEMS cannot be simply viewed as a smaller MEMS. Just like previously illustrated in the difference between macro and microdevices, there is effectively an effect of scaling factor that changes the dominant roles between classical physical effects but the novelty here is that additionally other effects rise like molecular or quantum effects.

I.2. NEMS: interest and features

NEMS cannot be considered only as smaller MEMS, i.e. as a natural extension of MEMS. The difference here is that they combine classical phenomena together with quantum and molecular effects. Actually, existing NEMS are generally more of mesoscopic type than purely nanoscaled. This means that they generally involve two dimensions (typically width and thickness) in the deep submicron range (hundreds of nm) and the third in the 1-10 μm range. However, although these devices are not strictly 'nano' regarding their dimensions, they feature specific phenomena that are effectively related to nanoscience: molecular recognition, adsorption/desorption processes, etc...

Existing NEMS could be classified between quasi-static and resonant NEMS [7]: the most versatile and widely used NEMS are vibrating singly- (cantilever) or doubly-clamped beams (bridge). In section III, resonating N/MEMS will be emphasized.

Compared to MEMS, NEMS have smaller area and volume but the resulting ratio area/volume is increased (see Table I - 1). In this sense, surface effects (roughness, adsorption, native oxides, and impurities) become more significant and influence the dynamic response through the Q-factor. In some cases, proximity forces like van der Waals or Casimir can start being more pronounced.

In terms of integration, the density can be increased by two or three orders of magnitude with respect to MEMS. Furthermore, 'true' nanodevices, whose all dimensions are submicronic, could ever be integrated in the IC itself in convergence with nano/microelectronics circuits. Otherwise, more classical post-CMOS integrations provide the same advantages as for MEMS in the sense that parasitic loading is much reduced.

One important question to answer is to what extent continuum mechanics can be applied to describe the mechanical behavior of NEMS. It appears from molecular dynamics (MD) simulations that for structures with a cross-sectional area larger than few nm^2 continuum approximations are still mostly valid [7, 8]. If a further refinement of the mechanical modeling of mesoscopic structures was pursued, the first improvement would consist in not using bulk material properties but MD corrected ones.

NEMS operated as high-frequency resonators feature unprecedented attributes from both technical and scientific points of view: with dimensions in the deep sub-micron, they exhibit extremely high fundamental resonance frequencies in the microwaves, very low active masses in the femtograms and relatively high quality factors (Q-factor) around 10^3-10^4.

These properties make NEMS suitable for a wide range of technological applications such as ultra sensitive [9] and fast sensors, actuators and signal processing components. Mechanically based data storage using NEMS has been pursued for some years: IBM Zürich [10] was a pioneer some years ago with the ‘Millipede’ device, an array of AFM cantilevers that provides gigabit storage at high data rate. Since then, other nanomechanical memory elements relying on mechanical bistability have been reported: one approach consisting in using the hysteretic non-linear behavior of nanobridges [11, 12], the other in implementing a SiO_2 floating beam to form a high speed (1 GHz) nonvolatile memory cell [13].

For scientific purposes, NEMS open up the exploration of new topics like the quantum behavior of mesoscopic mechanical systems. A manifestation of quantum mechanics on such systems is claimed to have been observed [14-16].

The development of NEMS devices and technology is carried out worldwide following very different orientations. However, it faces nowadays two major challenges: the establishment of cheap and reproducible nanofabrication techniques and the development of more accurate transducing methods adapted to nanoscale devices

II. Nanopatterning techniques overview

Since its early development, the semiconductor microelectronics industry has been using photolithography as a way to pattern the diverse structural layers of integrated circuits. A photolithography process flow implies coating the substrate with a photosensitive resist by spinning or spraying, exposing it to UV light through a mask containing chromium opaque patterns, either in contact or by projection, and finally developing the resist (in positive resists, exposed areas are dissolved by the development, in negative ones non-exposed areas are dissolved). In this way, 1-2 μm line-widths are routinely achieved [17]. Along the years, the resolution of photolithography has continuously been improved [17] through the use of (i) shorter wavelength in projection exposure tools, and (ii) optimized resists and masks. The patterning of sub-100 nm features constitutes a threshold where diffraction issues appear to be the main limitation. However, further decreasing the wavelength to circumvent this issue does not represent the ideal solution: smaller wavelengths are actually strongly absorbed in many materials what requires the use of new resists, masks and processing techniques in general.

The most modern implementation of photolithography already in industry is deep UV (DUV) lithography that achieves 65 nm resolution with 193 nm wavelength thanks to a reduction lens system. Other improvements of optical lithography are immersion lithography, occurring in a liquid environment, and extreme UV (EUV). All these techniques have in common extremely high investment costs both for the exposure system and the related tools, resists and masks.

High-resolution (100 nm) alternative techniques are X-ray and Laser-Interference (LIL) lithography. In the first one, the problem comes from the complicated mask fabrication process as no image reduction is possible so that the mask must be a 1:1 replica. The second one is limited to periodic patterns only.

Charged particle beams lithography, namely electron beam (eBL) and ion beam (iBL) lithography, are other well-known techniques. They are maskless direct writing systems that use a narrow beam to expose the patterns in a charge sensitive resist writing sequentially, point by point. This means that no mask is involved and the pattern is originally computer-stored and directly written through the fine spatial control of the beam. A main advantage here is that the beam particle, in particular electrons, are not limited by diffraction effects, however the sequential patterning limits considerably the throughput. To circumvent this limitation, efforts are underway to design projection lithography systems that generate in parallel thousands of charged particle beams (see www.charpan.com). In chapter 4, eBL is presented in more detail.

Both the microelectronics industry, looking forward defining sub-100 nm transistors, and nanotechnology, pursuing the definition of NEMS or materials-related applications, require new alternative nanopatterning techniques.

One reason is the cost. The development of a new method for the low cost parallel definition of sub-100 nm patterns is actively pursued. In topics not specifically related to IC, a second direction consists in proposing other approaches than resist based lithography. In applications involving chemically functionalized surfaces, a cyclic process based on the use of resist is not optimum as the surface is continuously chemically treated. Also related to the use of resist, non-planar substrates with more or less pronounced topographies are difficult to coat uniformly what makes the exposure more delicate. Another reason that guides the development of

new nanopatterning methods is the need to structure ‘unconventional’ materials (for example organic materials for organic light emitting diode) on ‘unconventional’ surfaces (polymers, self-assembled monolayers).

These new techniques can be classified into three main types: nanoimprint lithography (NIL) [18-20], soft-lithography [21] (also named micro-contact printing) and MEMS-based nanopatterning. MEMS-based means actually that they use nano/micromachined Si frames as tools to perform local depositions of a patterning material; in this category we can distinguish the items for liquid nano/microdispensing [22, 23] and for vacuum nanostencil lithography (nSL) [24-26] consisting in depositing various solid materials. In Figure 1, the principle of NIL, soft-lithography and nSL is sketched taking as a reference the already well established eBL+lift-off process:

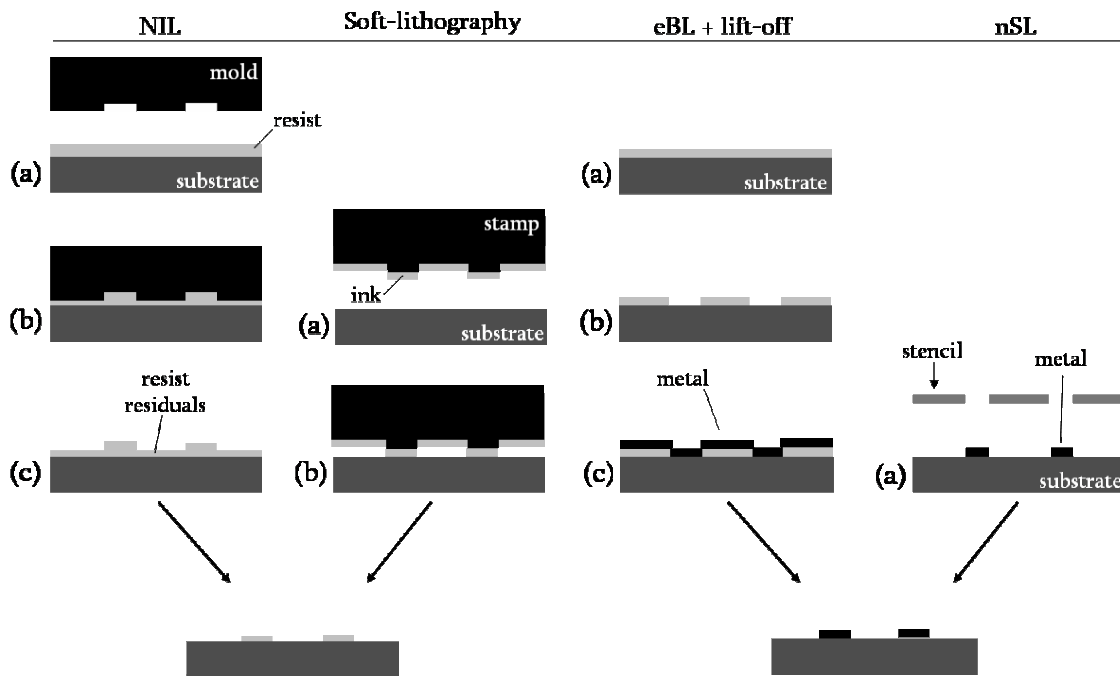

Figure 1. Schematic representations of the main alternative nanolithography techniques

The [eBL+lift-off] process consists in usually coating the substrate with PMMA (a), then this resist is exposed to the electron narrow beam and developed (b). After that, the top side of the substrate is metallized (c) with a metal thin layer (less than 50 nm thick). Finally, the sample in a resist dissolvent and the metal initially located on unexposed PMMA pillars is lifted-off what results in a structured surface with local nano/micropatterns.

In contrast to this process, the other three novel techniques are parallel. In NIL, a mold (a), generally defined previously by eBL and reactive ion etching (RIE), is pressed by hard contact onto a polymer resist [27] (b), what produces indentations (c). At this step, the resist is hardened by thermal or UV annealing and the unavoidable residuals remaining in-between the patterns are removed in general by an oxygen plasma etching. NIL can be applied according to a step-and-repeat approach with small molds and at full-wafer scale with wafer-sized molds. The problem here is the density of patterns in the mold and the ability of the system to apply a constant pressure all over the mold.

Micro-contact printing consists in fitting a stamp (a), in general made of PDMS, with ink and then in pressing it by soft-contact onto the surface (b). Compared to NIL, whose resolution has been demonstrated down to 10 nm, the resolution of soft-lithography lies more in the 100 nm range. The resulting pattern is very thin what makes difficult to implement it as an etch mask, however this technique can circumvent the issue of non-planar substrates.

Nano/micro dispensing techniques (not depicted here) of liquid sessile (i.e. attached) droplets (see chapter 6) face a major development for about ten years. The application of these non-lithographic techniques (for example dip-pen lithography [28]) lies mainly in biological assays and refilling of micro/nanofluidics networks.

Finally, the third alternative nanopatterning method is nanostencil lithography (nSL) and is one of the main topics of this thesis. As Figure 1 illustrates it, the principle of this technique is relatively simple. Its implementation is straightforward and requires less process steps compared to other approaches. It is a shadow-mask based parallel technique capable of patterning a full wafer with mesoscopic structures in one single deposition step. In the last few years, its resolution has been continuously pushed down and sub-50 nm patterns have been demonstrated [29].

A major advantage of nSL comes from the fact that it is a resistless non-contact method. In this sense, chemically functionalized and mechanically fragile surfaces can be structured with a wide, potentially unlimited, range of materials. Until a certain limit, surfaces with topography can also be patterned.

Nanostencil lithography is precisely described in chapter 4 and in the framework of this thesis it has been applied to the full-wafer patterning of nano/micromechanical devices on pre-fabricated CMOS substrates.

III. Nano/micromechanical resonators. Interest and physical features

Nano/micromechanical structures operated in static or dynamic (resonant) mode are potentially extremely versatile sensors depending on the way they are implemented and detected. Very diverse signal domains like magnetic, thermal, electrical, chemical, mechanical, etc... can be transduced with the same structure. In the late 90s, different authors [30, 31] pioneered the development of micromechanical-based multi-sensors taking advantage of scanning probes with nanoscale tip apex. Since then, diverse sensors based on nano/microstructures have been reported.

Nano/micromechanical structures can also be implemented as low-power low phase noise high-Q radio- (RF) and intermediate-frequency (IF) components [32, 33], in particular as filters and reference oscillators.

In all these resonating devices, electrical energy is converted into mechanical energy by exciting one resonant mode. The resulting displacement is then converted back directly (using for instance capacitive or piezoresistive detection schemes) or indirectly (for example optical transducing schemes) into an electrical signal.

Hereafter, a short survey of the different existing types of nano/micromechanical resonators is proposed. The key mechanisms playing upon the resonance quality factor and noise levels of such resonators are discussed. Finally, the main readout methods for the characterization of the frequency response are exposed.

III.1. Types of nano/micromechanical resonators

The most classical resonators are singly clamped beams, namely cantilevers. One reason for that is that because of their simple shape, they can be easily modeled. Actually, cantilevers have been extensively studied for a long time both in static (stress-related effects) and dynamic (effects of the viscosity of the surrounding medium) mode. They have been used for a long time for Scanning Probe Microscopy (SPM), consequently their further implementation as versatile sensors has been a natural evolution. In all resonators-based sensing applications, the detection scheme relies on monitoring the mechanical response that is modified by specific physical changes in the environment which can be further quantified.

Cantilevers operated in the quasi-static mechanical regime have been widely used to assess the adsorption of specific (through polymer or gold coating) and non-specific species onto the cantilever through the measurement of deflection changes related to adsorption-induced surface stress [34-43]: DNA hybridization (when the complementary strand links), glucose, alcohol and other odorant analytes have been successfully detected. The advantage of the static approach is that it can be performed in liquids as the viscosity of the environment is not an issue. However, one drawback associated to this approach is that the analyte must be located on one side only (what can be achieved functionalizing one side only).

In dynamic mode, cantilevers can potentially access more information. All the features of its frequency response give indications on external physical effects: resonance frequency shifts with respect to the eigenfrequency (natural resonance frequency, i.e. without any external force) and the value of the Q-factor [44, 45] can be related to the density and viscosity of the surrounding

fluid. Additionally, when some mass is deposited or adsorbed on it, the resulting frequency shift can be dissociated between a decreasing contribution related to the mass and another increasing one related to stiffness [46] or surface stress changes [34]. Some authors have actually measured simultaneously bending and resonance frequency changes [47, 48] to decorrelate these effects.

The other most reported nano/microresonators are flexural doubly clamped beams (bridges) [7, 49, 50], and paddles with doubly clamped beams [51, 52] that are operated in flexion and torsion. Nanowires and nanotubes seem to be promising ultra-high frequency mechanical resonators. A resonator operated in the bulk acoustic (longitudinal extension) mode [53] with high Q in air has also been demonstrated.

There exist other resonator shapes which are mostly implemented as RF components. In this category, Nguyen and coworkers [33] have promoted for fifteen years the use of MEMS as filters and reference clock oscillators with the target of achieving the highest possible product Q-factor per resonance frequency. These devices involve a broad range of shapes [33]: in particular comb capacitors transducers [54], free-free beams, wine-glass disks (Q=161000 at 62 MHz in vacuum), contour-mode disks (Q=10000 at 1.5 GHz) and radial-mode disks (Q=1500 at 1.14 GHz). Arrays of coupled resonators that form programmable band-pass filters have also been demonstrated. All these devices are very interesting for two reasons: first they illustrate very well the assumption that structures supported at resonance nodes rather than at their extremities minimize drastically anchor losses and achieve high Q. Second, they show that a miniaturization towards nanometer scale is not always directly the best solution to achieve high frequencies, in particular for power handling issues (the interface with micro and macro-components is difficult in terms of impedance matching).

This overview will end with the thin-film bulk acoustic resonator (FBAR). This is actually the type of MEMS that is equivalent to bulk acoustic wave macro-resonators (typically quartz-crystal resonators). Structurally, this is a parallel plate capacitor sandwiching a piezoelectric dielectric thin film. An alternate signal applied at the electrodes provokes bulk vibrational modes in the piezo-film. Very high Q-factors are obtained for frequencies in the GHz range minimizing anchors losses by releasing the membrane. Commercially available devices [55] are already in the market.

III.2. Mechanisms determining the quality factor and the noise

A given resonance mode is characterized by (i) its resonance frequency, (ii) its amplitude and shape and (iii) its quality factor Q. Regarding the design and the operation of nano/micromechanical structures, it is important to assess, at least qualitatively, what are the dominant physical phenomena behind the Q-factor. For sensing and actuating purposes, maximizing the Q-factor is systematically an objective to pursue to improve the resolution and lower the noise.

Physically, the Q-factor can be understood as the ratio between the total elastic energy stored in one vibration cycle and the dissipated energy during this cycle, what is approximately equivalent to the ratio between f_0 the resonance frequency and Δf the bandwidth at -3 dB (at the maximum amplitude divided by √2):

$$\boldsymbol{Q} = 2\pi \frac{\boldsymbol{E}}{\Delta \boldsymbol{E}} \approx \frac{\boldsymbol{f}_0}{\Delta \boldsymbol{f}} \qquad \text{(I.1)}$$

In practice, the Q can be extracted from the resonance spectrum, for example fitting it with a Lorentz function, or can be obtained through the implementation of the "ring-down" technique [56, 57] that consists in brusquely stopping the driving and in monitoring the amplitude decay. Fitting the obtained curve to an exponential one, the Q can be obtained from the time constant τ_0 in this way: $Q = \pi \tau_0 f_0$.

It is always difficult to determine if energy dissipations affecting the resonance spectrum of the resonator are related to intrinsic or extrinsic processes caused by the detection set-up. The effective Q factor is the result of the combination of several losses mechanisms [57], in general the damping of the surrounding medium plays a key role but there are also clamping (anchor), thermoelastic, surface and volume-related effects:

$$\frac{1}{Q} = \sum_i \frac{1}{Q_i} = \frac{1}{Q_{CLAMPING}} + \frac{1}{Q_{THERMOELASTIC}} + \frac{1}{Q_{SURFACE}} + \frac{1}{Q_{VOLUME}} + \frac{1}{Q_{VISCOUS}} + \frac{1}{Q_{OTHERS}} \qquad \text{(I.2)}$$

Some energy losses are localized in resonators clamping anchors [57, 58]. For vertically vibrating cantilevers, Hosaka et al. [59] report that the related Q factor is approximately given by $Q_{CLAMPING} = 2.17\, l^3 / t^3$ (where l and t are the cantilever length and thickness). To get free of this type of loss, the resonators should be operated in torsional mode or as previously said, they should be supported at vibration nodes (i.e. null motion) and not at their ends.

When the resonator bends, thermoelastic dissipation (TED) [57, 58] is generated owing to the irreversible thermal flux that is created through the device between the compressed and strained sides. In thin resonators (equal or less than few microns), TED is expected to be negligible.

One point on which all experimental data are in agreement concerns surface related losses. Several authors [56-58, 60] have shown experimental measurements demonstrating a clear correlation between increasing surface/volume ratio (when down scaling the devices) and lower Q factors (in [60], the authors even report a linear trend between both).

Internal losses, related to volume effects, are very difficult to model, however some authors [58] attribute these losses to phonon interactions between structural internal defects (charged impurities). Nano/micromechanical resonators are frequently coated with metal layers to ensure electrical conduction: in this sense the effect of the amount of deposited metal on the Q factor is investigated [52]. Metals are known to have important internal frictions and it has been experimentally confirmed that the Q-factor decreases with increasing deposited thickness.

The last main contribution is the damping of the surrounding medium, namely viscous losses. This effect is the one that is maybe the most analytically assessed [45]. For resonators exhibiting Q<100 000, a saturation in the enhancement of the Q factor is generally observed below pressure levels comprised between 0.1 and 1 mBar [58, 61].

Improving the quality factor of a mechanical structure is not straightforward. However, some guidelines could be the use of (i) crystalline materials as structural materials to reduce internal losses, (ii) surface treatments to passivate the surface in order to suppress free chemical bonds and (iii) a refined mechanical analysis to place adequately the supporting points of the vibrating structure (to reduce clamping-related losses). Surface thermal treatments have yet demonstrated to be effective only in a limited timeframe [57]. Another way recently illustrated in [62, 63] is to use highly strained structures (the exact explication for this is not yet agreed).

With regard to these matters, the fluctuation-dissipation theorem (known as Nyquist-Johnson theorem in electrical circuits) indicates that systems which dissipate energy are necessarily sources of noise [64]. For all kinds of sensing applications implementing resonators in dynamic mode, the frequency stability is an important feature governed both by extrinsic (from the transducer and the readout circuitry) and by intrinsic (related to the nanomechanical part itself) processes [65]. In macro and micro-elements, it is generally considered that the noise is determined by extrinsic processes. In contrast, in nanodevices the fluctuations related to higher sensing sensitivity and ultra-sensitive integrated transducing schemes are likely to become predominant over extrinsic processes.

Focusing on intrinsic processes, three main sources of noise affect the nanoresonator: thermomechanical, temperature and adsorption/desorption fluctuations [64].

Thermomechanical noise is generated because of the thermally driven random motion of the mechanical device:

$$\frac{1}{2} m_{EFF}\, \omega_0^2 \left\langle x_{TH}^2 \right\rangle = \frac{1}{2} k_B T \qquad \text{(I.3)}$$

where m_{EFF}, ω_0, x_{TH}, k_B and T are respectively the resonator effective mass, the angular resonance frequency, the thermally driven mean-square displacement of the resonator, the Boltzmann constant and the temperature. In fact, the displacement noise also causes frequency fluctuations. The exact calculation depends from the type of readout scheme, either closed or open loop. In any case, this source is generally considered as the dominant one among intrinsic processes.

Because of their small heat capacity [65], NEMS face rather large temperature fluctuations. Since the resonator dimensions and material properties are both temperature dependent, this type of fluctuation will also convert into frequency fluctuations. This trend should amplify in ultra-small devices whose temperature should be lowered to diminish these effects.

Finally, the third main intrinsic noise process is related to permanent adsorption/desorption phenomena taking place on the resonator surface. Indeed, gas molecules located in the vicinity of the resonator constantly adsorb and desorb from its surface, i.e. mass load or unload it, and therefore create permanent resonance frequency fluctuations. This phenomenon is a surface effect; surface passivation should help in reducing the binding energy between gas molecules and the surface.

III.3. Characterization techniques of frequency response

To characterize either the static or the dynamic mechanical response of nano/ micromechanical resonators, several techniques have been reported. We propose to classify them into two categories: (i) techniques requiring an external set-up that cannot be easily miniaturized and integrated on-chip and (ii) techniques that can potentially be integrated on-chip.

In the first category, three main approaches emerge. The first, maybe the most expanded one, relies on optical methods. There exists (i) interference techniques [51, 52, 66-68] based on the Fabry-Pérot interferometer formed by the stack resonator/air gap/substrate and (ii) AFM-based set-up [35, 39, 69] which monitor the reflection of a laser beam off the resonator with a position sensitive photodiode. Resonator deflection is detected through the modification of the impact

point of the beam on the photodiode. The obtained resolution in motion is in the tenth of nanometer, however the micron range size of the laser spot limits the minimum size of the resonator. More generally, the relatively heavy set-up together with the required alignment step between the beam and the resonator constitute serious drawbacks if a portable implementation of the sensor is pursued. The samples measured with an optical technique can be actuated in many different ways: electrostatic (direct [51, 66] or parametric [70]), thermal [71, 72], or piezoelectric [69].

A second important detection methods relies on driving the resonator through the Lorentz force applying a magnetic field and passing a current across the resonator (magnetomotive approach). The resulting motion develops an electromotive voltage whose associated impedance depends upon the oscillation amplitude. Directly measuring this voltage [7, 49, 50, 64, 73] allows accessing the frequency response of the resonator. This method can be applied to almost any structure, its drawback arises from the heavy set-up requiring high magnetic fields. In the same order, resonator with a magnetic structural layer have directly been oscillated applying a time-varying magnetic field. This approach is too restrictive since only resonators fabricated with a magnetic material can be driven.

A third non portable method consists in using atomic force microscopy (AFM) to characterize the dynamic mechanical frequency response. In [74], the AFM is operated in dynamic non-contact mode to study the resonance of a cantilever. In this low force regime, the oscillation amplitudes are registered maintaining the tip at a fix position sweeping laterally. Constantly (but slowly) varying the driving frequency, a resonance 'image' is formed. In [75, 76], GHz oscillations of thin-film bulk acoustic resonators (FBAR) are studied according to a different procedure: the AFM tip is placed in contact. A modulated driving signal allows detecting low frequency oscillation amplitudes by means of a lock-in detection technique while driving (electrostatically) the FBAR at GHz frequencies. This method allows determining mode shapes and resonance frequencies in the GHz range. In the framework of this thesis, some preliminary work detailed in annex A.9 has been undertaken at INL (INSA Lyon) to use AFM as a versatile characterization technique of NEMS.

In the second category, we consider electrical readout techniques: piezoelectric [77], capacitive [33, 53, 54, 78-80] and piezoresistive [31, 61, 81, 82]. In N-MEMS, these last two are widely used. Piezoresistive detection is a smart solution that takes advantages of the high gauge factor provided by doped silicon. Basically, the deflection motion generates a change in the piezoresistor resistance. Placing such piezoresistors on a target resonator and on a reference non-driven one, a Wheatstone bridge can be formed to monitor the bending dependent differential output voltage. The principle of the capacitive method is relatively simple and easy to implement as well: the resonator is placed in front of a fixed driving electrode. The parallel plate capacitance thus formed is continuously measured (through its voltage or its current) while driven with an alternate voltage. Around resonance, a mechanical motion appears and modifies the gap between the two plates: a new component of the capacitive current (named motional current) is generated. It is specifically originated by the mechanical motion and maximized at the resonance frequency. This approach is the topic of this thesis and is going to be detailed in chapters 2 and 3.

Following one of these three approaches, smart and portable devices can be fabricated for sensing or actuating applications.

IV. NEMS-based mass sensors

Nano/micromechanical resonators offer outstanding perspectives to measure ultra-small amounts of mass deposited on them. In the last decade, mass measurements based on resonating nano/microdevices have been a subject of growing interest. The principle of operation is based on the detection of the shift of resonance frequency when a small quantity of mass is deposited on top of the mechanical structure. In general, the smaller the resonator, the more sensitive it is because the relative change of mass is greater.

The reference device used for the purpose of measuring small masses, for example to monitor the deposition of thin layers in the semiconductor industry, is the commercially available quartz crystal microbalance (QCM). With respect to it, micro and nanomechanical resonators may offer drastic advantages in terms of mass sensitivity and system integration. In addition, their small size ensures intrinsically a high spatial resolution.

Hereafter, the basic features of a QCM are described and a survey of implementations of nano/micromechanical resonators as ultra-sensitive mass sensors is proposed. In direct connection with these studies, chapter 6 will present a series of mass sensing experiments based upon NEMS which all use this sensitivity attribute for other purposes than just measuring a small mass. Additionally, a comparison of the performance of QCM and nano/microdevices we have been fabricating will be carried out based on experimental results.

IV.1. Quartz-crystal microbalances: applications and performance

Owing to their mechanical, electrical and chemical properties, quartz crystals are widely used piezoelectric devices that are very adequate for applications requiring well-controlled frequencies. They are mostly applied as controlling element in reference clock oscillating circuits and as precision microbalances. Due to their piezoelectricity, the application of an alternate voltage on two opposite sides creates bulk acoustic waves resulting in high-Q and high resonance frequency modes.

Quartz-crystal microbalances consist of a thin quartz disc sandwiched between a pair of electrodes. They have been used for a long time to monitor thin film deposition [83, 84] under vacuum or gaseous environments. The development of QCM systems (see for example www.q-sense.com) for use in fluids or with visco-elastic deposits has dramatically increased the number of applications. In this sense, QCM also serve now to explore the electrochemistry of interfacial processes at electrode surfaces.

The main features of a QCM are an areal mass sensitivity of $1.2\ 10^{-8}\ g.cm^{-2}.Hz^{-1}$ and a classical and optimum frequency resolution of 0.1 and 0.005 Hz respectively (www.inficon.com). In chapter 6, the theory of operation of a quartz-crystal with the aim of measuring ultra-thin (subatomic) gold layer thicknesses will be described.

IV.2. State-of-the-art of mass sensors based on micro/nanomechanical resonators

In this section, a brief survey of existing NEMS-based mass sensors is exposed. According to criteria of mass sensitivity and minimum mass resolution (mass noise floor), we report in Table I -

2 some of the most relevant (according to our opinion) NEMS-based mass sensing experiments we are aware of and discuss them. Then the main applications, the experimental procedure and different ways to improve the mass sensor are discussed.

Research group & year	f_{RES} (MHz)	S (g.Hz-1)	δm (g) (deposited)	resolution (10^{-18}g)	deposited material	conditions
Caltech [9] 2006	190	$0.62\ 10^{-21}$ (zepto)	$100\ 10^{-21}$	0.02	N_2 (areal)	SiC bridge in ultra-high vacuum at 37 K
Caltech [49] 2004	32.8	$0.39\ 10^{-18}$ (atto)	$40\ 10^{-18}$	2.5	Au (areal)	SiC bridge in ultra-high vacuum at 17 K
Cornell [85] 2004	13.3	$\approx 0.1\ 10^{-18}$ (atto)	$\approx 10\ 10^{-18}$	0.4	Thiolate SAM (punctual)	Polysilicon paddles measured at $3\ 10^{-6}$ Torr
Caltech [81] 2007	127	$1.4\ 10^{-21}$ (zepto)	$1\ 10^{-18}$	≈ 0.1 (in air)	chemisorption of di-fluoroethane (areal)	SiC nanocantilevers with metallic piezoresistive layer measured in air
UAB [86] 2007	1.3	$0.9\ 10^{-18}$ (atto)	$1.4\ 10^{-15}$	12	Au (areal)	CMOS metal cantilever in vacuum ($6\ 10^{-7}$ mBar)

Table I - 2. Main features of five state-of-the art NEMS-based mass sensing experiments in terms of resonance frequency (f_{RES}), mass sensitivity (S), reported deposited mass (δm), mass noise floor, deposited material and specific conditions (device, environment, etc...)

The Caltech group (USA) [7, 9, 49, 65] is a leader in this topic and used to apply magnetomotive actuation and electromotive voltage detection schemes in cryogenic chambers (low temperatures and ultra-high vacuum). In [9], the authors suggest that NEMS can potentially provide a one Dalton (mass of a carbon atom) resolution. In [81], they use SiC cantilevers coated with a metallic piezoresistive layer for ultra-sensitive low noise measurements in air. In all the experiments, SiC bridges are embedded in a phase-locked loop (PLL) to directly track the resonance frequency and thereby the shifts related to mass loading.

At Cornell university (USA) [85, 87], they use paddle nanoresonators with optical detection and at UAB (Spain) [86] smart CMOS cantilevers in a capacitive scheme. In those papers, both groups have calibrated the mass sensing performance of their sensor respectively (i) removing a gold accretion of well-known mass (Cornell) and (ii) depositing a MgF_2 layer of well-known thickness (UAB).

The applications provided by this high-resolution mass sensing concept are multiple. Ultimately, the fact of continuously pushing down the mass sensitivity and resolution will allow studying theoretical physical and chemical surface phenomena through the monitoring of the adsorption and desorption of molecules on a surface. Bio-chemical, -medical and-technological applications are very promising, in particular to study molecular interactions. A group of the university of Basel (Switzerland) together with IBM Zürich [37-39, 47, 69] are very active in this field. In [69], they get to measure time-resolved adsorption of small masses based on protein-ligand interactions. For more industrial objectives, such sensors can likely replace in a future QCM to monitor the deposition of thin layers in vacuum in evaporation systems, or in FIB-aided depositions [88].

Depositing a mass on top of a nano/micromechanical resonator results in a resonance frequency shift that is a combination of three contributions: (i) a mass loading leading to a frequency decrease (this is the most general approach in first approximation), but also (ii) a

stiffening effect of the resonating structure caused by the adsorbate [46] and (iii) and an adsorption-induced surface stress [34] which both tend to increase the frequency. In some specific applications, the mass loading effect dominates over the others two: (i) depositing sub-monolayer areal accretions, or (ii) placing a punctual mass accretion at the maximum deflection point [46, 89], or (iii) using low-stress deposition materials.

Concerning the detection technique, capacitive readout seems to generate less temperature fluctuations than optical detection since the laser beam provokes a local heating effect [90], [91]. Electrical mass sensors, either CMOS integrated [78, 86] or discrete [92] capacitive devices and piezoresistive cantilevers [81], relax alignment requirements and may be potentially packaged as portable sensors.

To improve the NEMS-based mass sensing concept in terms of mass sensitivity and mass resolution, several approaches have been proposed. To enhance the sensitivity, Spletzer et al. [93] use mechanically coupled microcantilevers and basing on Anderson mode localization theory, they show that using such devices the relative change in amplitude is much bigger (two-three orders of magnitude) than the relative resonance frequency shifts (what is usually measured), furthermore the amplitude change is relatively independent of Q-factor changes and is quite insensitive to environmental drifts common to both cantilevers. In [94], [95] and [96], the authors insist that both the Q-factor and the mass sensitivity are enhanced using higher resonance modes, either flexural or torsional, provided the deposit is not located at nodal points (i.e. of minimum motion). In [97], the author demonstrates theoretically the intuitive assumption that operating the mass sensor at the onset of the mechanical nonlinear regime ensures a very high sensitivity since the slope is almost infinite at this point. In [98], the authors compare different resonator structural materials (among the ones classically available in a MEMS foundry: Al, Si, Ti, Au, etc..): at constant spring constant, thickness and width, they demonstrate that Al offers the best mass sensitivity. Finally, the authors in [99] study the influence of the resonator shape and suggest that increasing the I/A ratio (moment of inertia and the cross-section respectively) can help in decreasing the mass noise floor. With regard to this matter, they propose a simplified technological process flow that creates a double-triangle cross section, e.g. with a better I/A ratio.

Bibliographical references

1. Petersen, K.E.
Silicon as a mechanical material
Proceedings of the IEEE, 1982. **70**(5): p. 420-457.

2. Bao, M.-H.
Micro Mechanical Transducers
Elsevier ed, Vol. 8, 2000, Amsterdam.

3. Rebeiz, G.
RF MEMS Theory, design and technology
Wiley ed, 2003.

4. Ma, W., R.Q. Zhu, L. Rufer, Y. Zohar, and M. Wong
An integrated floating-electrode electric microgenerator
Journal of Microelectromechanical Systems, 2007. **16**(1): p. 29-37.

5. Binnig, G. and H. Rohrer
Scanning Tunneling Microscopy
Surface Science, 1983. **126**(1-3): p. 236-244.

6. Binnig, G., C. Gerber, E. Stoll, T.R. Albrecht, and C.F. Quate
Atomic Resolution with Atomic Force Microscope
Europhysics Letters, 1987. **3**(12): p. 1281-1286.

7. Ekinci, K.L. and M.L. Roukes
Nanoelectromechanical systems
Review of Scientific Instruments, 2005. **76**(6).

8. Tang, Z., Y. Xu, G. Li, and N.R. Aluru
Physical models for coupled electromechanical analysis of silicon nanoelectromechanical systems
Journal of Applied Physics, 2005. **97**(11).

9. Yang, Y.T., C. Callegari, X.L. Feng, K.L. Ekinci, and M.L. Roukes
Zeptogram-scale nanomechanical mass sensing
Nano Letters, 2006. **6**(4): p. 583-586.

10. Vettiger, P., J. Brugger, M. Despont, U. Drechsler, U. Durig, W. Haberle, M. Lutwyche, H. Rothuizen, R. Stutz, R. Widmer, and G. Binnig
Ultrahigh density, high-data-rate NEMS-based AFM data storage system
Microelectronic Engineering, 1999. **46**(1-4): p. 11-17.

11. Badzey, R.L. and P. Mohanty
Coherent signal amplification in bistable nanomechanical oscillators by stochastic resonance
Nature, 2005. **437**(7061): p. 995-998.

12. Badzey, R.L., G. Zolfagharkhani, A. Gaidarzhy, and P. Mohanty
A controllable nanomechanical memory element
Applied Physics Letters, 2004. **85**(16): p. 3587-3589.

13. Tsuchiya, Y., K. Takai, N. Momo, T. Nagami, H. Mizuta, S. Oda, S. Yamaguchi, and T. Shimada
Nanoelectromechanical nonvolatile memory device incorporating nanocrystalline Si dots
Journal of Applied Physics, 2006. **100**(9).

14. Schwab, K.C., M.P. Blencowe, M.L. Roukes, A.N. Cleland, S.M. Girvin, G.J. Milburn, and K.L. Ekinci
Comment on "Evidence for quantized displacement in macroscopic nanomechanical oscillators"
Physical Review Letters, 2005. **95**(24).

15. Gaidarzhy, A., G. Zolfagharkhani, R.L. Badzey, and P. Mohanty
Comment on "Evidence for quantized displacement in macroscopic nanomechanical oscillators" - Reply
Physical Review Letters, 2005. **95**(24).

16. Gaidarzhy, A., G. Zolfagharkhani, R.L. Badzey, and P. Mohanty
Evidence for quantized displacement in macroscopic nanomechanical oscillators
Physical Review Letters, 2005. **94**(3).

17. Madou, M.J.
Fundamentals of Microfabrication, the Science of Miniaturization (2nd ed.)
CRC Press ed, 2002.

18. Chou, S.Y., P.R. Krauss, and P.J. Renstrom
Nanoimprint lithography
Journal of Vacuum Science & Technology B, 1996. **14**(6): p. 4129-4133.

19. Chou, S.Y., P.R. Krauss, and P.J. Renstrom
Imprint lithography with 25-nanometer resolution
Science, 1996. **272**(5258): p. 85-87.

20. Chou, S.Y., P.R. Krauss, and P.J. Renstrom
Imprint of Sub-25 Nm Vias and Trenches in Polymers
Applied Physics Letters, 1995. **67**(21): p. 3114-3116.

21. Xia, Y.N. and G.M. Whitesides
Soft lithography
Annual Review of Materials Science, 1998. **28**: p. 153-184.

22. Fang, A.P., E. Dujardin, and T. Ondarcuhu
Control of droplet size in liquid nanodispensing
Nano Letters, 2006. **6**(10): p. 2368-2374.

23. Meister, A., M. Liley, J. Brugger, R. Pugin, and H. Heinzelmann
Nanodispenser for attoliter volume deposition using atomic force microscopy probes modified by focused-ion-beam milling
Applied Physics Letters, 2004. **85**(25): p. 6260-6262.

24. Brugger, J., J.W. Berenschot, S. Kuiper, W. Nijdam, B. Otter, and M. Elwenspoek
Resistless patterning of sub-micron structures by evaporation through nanostencils
Microelectronic Engineering, 2000. **53**(1-4): p. 403-405.

25. van den Boogaart, M.A.F.
Stencil lithography: an ancient technique for advanced micro- and nanopatterning
Hartung-Gorre Verlag ed, Series in Microsystems, Vol. 20, 2006, Konstanz.

26. van den Boogaart, M.A.F., G.M. Kim, R. Pellens, J.P. van den Heuvel, and J. Brugger
Deep-ultraviolet-microelectromechanicaI systems stencils for high-throughput resistless. patterning of mesoscopic structures
Journal of Vacuum Science & Technology B, 2004. **22**(6): p. 3174-3177.

27. Schift, H., L.J. Heyderman, M.A.D. Maur, and J. Gobrecht
Pattern formation in hot embossing of thin polymer films
Nanotechnology, 2001. **12**(2): p. 173-177.

28. Piner, R.D., J. Zhu, F. Xu, S.H. Hong, and C.A. Mirkin
"Dip-pen" nanolithography
Science, 1999. **283**(5402): p. 661-663.

29. Vazquez Mena, O., C.W. Park, M.A.F. van den Boogaart, and J. Brugger
Nanostencil lithography for nanowire patterning
in the proceedings of the *Nanoelectronics Days*. 2006. Aachen, Germany.

30. Berger, R., C. Gerber, H.P. Lang, and J.K. Gimzewski
Micromechanics: A toolbox for femtoscale science: "Towards a laboratory on a tip"
Microelectronic Engineering, 1997. **35**(1-4): p. 373-379.

31. Boisen, A., J. Thaysen, H. Jensenius, and O. Hansen
Environmental sensors based on micromachined cantilevers with integrated read-out
Ultramicroscopy, 2000. **82**(1-4): p. 11-16.

32. Motiee, M., R.R. Mansour, and A. Khajepour
Micromechanical resonators and filters for microelectromechanical system applications
Journal of Vacuum Science & Technology B, 2006. **24**(6): p. 2499-2508.

33. Nguyen, C.T.C.
MEMS technology for timing and frequency control
IEEE Transactions on Ultrasonics Ferroelectrics and Frequency Control, 2007. **54**(2): p. 251-270.

34. Chen, G.Y., T. Thundat, E.A. Wachter, and R.J. Warmack
Adsorption-Induced Surface Stress and Its Effects on Resonance Frequency of Microcantilevers
Journal of Applied Physics, 1995. **77**(8): p. 3618-3622.

35. Fritz, J., M.K. Baller, H.P. Lang, H. Rothuizen, P. Vettiger, E. Meyer, H.J. Guntherodt, C. Gerber, and J.K. Gimzewski
Translating biomolecular recognition into nanomechanics
Science, 2000. **288**(5464): p. 316-318.

36. Fritz, J., M.K. Baller, H.P. Lang, T. Strunz, E. Meyer, H.J. Guntherodt, E. Delamarche, C. Gerber, and J.K. Gimzewski
Stress at the solid-liquid interface of self-assembled monolayers on gold investigated with a nanomechanical sensor
Langmuir, 2000. **16**(25): p. 9694-9696.

37. Lang, H.P., M.K. Baller, R. Berger, C. Gerber, J.K. Gimzewski, F.M. Battiston, P. Fornaro, J.P. Ramseyer, E. Meyer, and H.J. Guntherodt
An artificial nose based on a micromechanical cantilever array
Analytica Chimica Acta, 1999. **393**(1-3): p. 59-65.

38. Lang, H.P., M. Hegner, and C. Gerber
Nanomechanics - The link to biology and chemistry
Chimia, 2002. **56**(10): p. 515-519.

39. Lang, H.P., M. Hegner, E. Meyer, and C. Gerber
Nanomechanics from atomic resolution to molecular recognition based on atomic force microscopy technology
Nanotechnology, 2002. **13**(5): p. R29-R36.

40. Pei, J.H., F. Tian, and T. Thundat
Glucose biosensor based on the microcantilever
Analytical Chemistry, 2004. **76**(2): p. 292-297.

41. Hu, Z.Y., T. Thundat, and R.J. Warmack
Investigation of adsorption and absorption-induced stresses using microcantilever sensors
Journal of Applied Physics, 2001. **90**(1): p. 427-431.

42. Baller, M.K., H.P. Lang, J. Fritz, C. Gerber, J.K. Gimzewski, U. Drechsler, H. Rothuizen, M. Despont, P. Vettiger, F.M. Battiston, J.P. Ramseyer, P. Fornaro, E. Meyer, and H.J. Guntherodt
A cantilever array-based artificial nose
Ultramicroscopy, 2000. **82**(1-4): p. 1-9.

43. Dareing, D.W. and T. Thundat
Simulation of adsorption-induced stress of a microcantilever sensor
Journal of Applied Physics, 2005. **97**(4).

44. Chon, J.W.M., P. Mulvaney, and J.E. Sader
Experimental validation of theoretical models for the frequency response of atomic force microscope cantilever beams immersed in fluids
Journal of Applied Physics, 2000. **87**(8): p. 3978-3988.

45. Sader, J.E.
Frequency response of cantilever beams immersed in viscous fluids with applications to the atomic force microscope
Journal of Applied Physics, 1998. **84**(1): p. 64-76.

46. Tamayo, J., D. Ramos, J. Mertens, and M. Calleja
Effect of the adsorbate stiffness on the resonance response of microcantilever sensors
Applied Physics Letters, 2006. **89**(22).

47. Battiston, F.M., J.P. Ramseyer, H.P. Lang, M.K. Baller, C. Gerber, J.K. Gimzewski, E. Meyer, and H.J. Guntherodt
A chemical sensor based on a microfabricated cantilever array with simultaneous resonance-frequency and bending readout
Sensors and Actuators B-Chemical, 2001. **77**(1-2): p. 122-131.

48. Cherian, S. and T. Thundat
Determination of adsorption-induced variation in the spring constant of a microcantilever
Applied Physics Letters, 2002. **80**(12): p. 2219-2221.

49. Ekinci, K.L., X.M.H. Huang, and M.L. Roukes
Ultrasensitive nanoelectromechanical mass detection
Applied Physics Letters, 2004. **84**(22): p. 4469-4471.

50. Blick, R.H., A. Erbe, L. Pescini, A. Kraus, D.V. Scheible, F.W. Beil, E. Hoehberger, A. Hoerner, J. Kirschbaum, and H. Lorenz
Nanostructured silicon for studying fundamental aspects of nanomechanics
Journal of Physics-Condensed Matter, 2002. **14**(34): p. R905-R945.

51. Evoy, S., D.W. Carr, L. Sekaric, A. Olkhovets, J.M. Parpia, and H.G. Craighead
Nanofabrication and electrostatic operation of single-crystal silicon paddle oscillators
Journal of Applied Physics, 1999. **86**(11): p. 6072-6077.

52. Olkhovets, A., S. Evoy, D.W. Carr, J.M. Parpia, and H.G. Craighead
Actuation and internal friction of torsional nanomechanical silicon resonators
Journal of Vacuum Science & Technology B, 2000. **18**(6): p. 3549-3551.

53. Mattila, T., J. Kiihamaki, T. Lamminmaki, O. Jaakkola, P. Rantakari, A. Oja, H. Seppa, H. Kattelus, and I. Tittonen
A 12 MHz micromechanical bulk acoustic mode oscillator
Sensors and Actuators a-Physical, 2002. **101**(1-2): p. 1-9.

54. Nguyen, C.T.C. and R.T. Howe
An integrated CMOS micromechanical resonator high-Q oscillator
IEEE Journal of Solid-State Circuits, 1999. **34**(4): p. 440-455.

55. Ruby, R., P. Bradley, J. Larson, III, Y. Oshmyansky, and D. Figueredo
Ultra-miniature high-Q filters and duplexers using FBAR technology
in the proceedings of the *IEEE International Solid-State Circuits Conference*. 2001.

56. Ono, T. and M. Esashi
Effect of ion attachment on mechanical dissipation of a resonator
Applied Physics Letters, 2005. **87**(4).

57. Yasumura, K.Y., T.D. Stowe, E.M. Chow, T. Pfafman, T.W. Kenny, B.C. Stipe, and D. Rugar
Quality factors in micron- and submicron-thick cantilevers
IEEE Journal of Microelectromechanical Systems, 2000. **9**(1): p. 117-125.

58. Mohanty, P., D.A. Harrington, K.L. Ekinci, Y.T. Yang, M.J. Murphy, and M.L. Roukes
Intrinsic dissipation in high-frequency micromechanical resonators
Physical Review B, 2002. **66**(8).

59. Hosaka, H., K. Itao, and S. Kuroda
Damping Characteristics of Beam-Shaped Micro-Oscillators
Sensors and Actuators a-Physical, 1995. **49**(1-2): p. 87-95.

60. Carr, D.W., S. Evoy, L. Sekaric, H.G. Craighead, and J.M. Parpia
Measurement of mechanical resonance and losses in nanometer scale silicon wires
Applied Physics Letters, 1999. **75**(7): p. 920-922.

61. Xu, Y., J.T. Lin, B.W. Alphenaar, and R.S. Keynton
Viscous damping of microresonators for gas composition analysis
Applied Physics Letters, 2006. **88**(14).

62. Cimalla, V., C. Foerster, F. Will, K. Tonisch, K. Brueckner, R. Stephan, M.E. Hein, O. Ambacher, and E. Aperathitis
Pulsed mode operation of strained microelectromechanical resonators in air
Applied Physics Letters, 2006. **88**(25).

63. Verbridge, S.S., J.M. Parpia, R.B. Reichenbach, L.M. Bellan, and H.G. Craighead
High quality factor resonance at room temperature with nanostrings under high tensile stress
Journal of Applied Physics, 2006. **99**(12).

64. Cleland, A.N. and M.L. Roukes
Noise processes in nanomechanical resonators
Journal of Applied Physics, 2002. **92**(5): p. 2758-2769.

65. Ekinci, K.L., Y.T. Yang, and M.L. Roukes
Ultimate limits to inertial mass sensing based upon nanoelectromechanical systems
Journal of Applied Physics, 2004. **95**(5): p. 2682-2689.

66. Carr, D.W. and H.G. Craighead
Fabrication of nanoelectromechanical systems in single crystal silicon using silicon on insulator substrates and electron beam lithography
Journal of Vacuum Science & Technology B, 1997. **15**(6): p. 2760-2763.

67. Carr, D.W., L. Sekaric, and H.G. Craighead
Measurement of nanomechanical resonant structures in single-crystal silicon
Journal of Vacuum Science & Technology B, 1998. **16**(6): p. 3821-3824.

68. Karabacak, D., T. Kouh, and K.L. Ekinci
Analysis of optical interferometric displacement detection in nanoelectromechanical systems
Journal of Applied Physics, 2005. **98**(12).

69. Braun, T., V. Barwich, M.K. Ghatkesar, A.H. Bredekamp, C. Gerber, M. Hegner, and H.P. Lang
Micromechanical mass sensors for biomolecular detection in a physiological environment
Physical Review E, 2005. **72**(3).

70. Carr, D.W., S. Evoy, L. Sekaric, H.G. Craighead, and J.M. Parpia
Parametric amplification in a torsional microresonator
Applied Physics Letters, 2000. **77**(10): p. 1545-1547.

71. Sekaric, L., M. Zalalutdinov, S.W. Turner, A.T. Zehnder, J.M. Parpia, and H.G. Craighead
Nanomechanical resonant structures as tunable passive modulators of light
Applied Physics Letters, 2002. **80**(19): p. 3617-3619.

72. Ilic, B., S. Krylov, K. Aubin, R. Reichenbach, and H.G. Craighead
Optical excitation of nanoelectromechanical oscillators
Applied Physics Letters, 2005. **86**(19).

73. Beil, F.W., L. Pescini, E. Hohberger, A. Kraus, A. Erbe, and R.H. Blick
Comparing schemes of displacement detection and subharmonic generation in nanomachined mechanical resonators
Nanotechnology, 2003. **14**(7): p. 799-802.

74. Abadal, G., Z.J. Davis, X. Borrise, O. Hansen, A. Boisen, N. Barniol, F. Perez-Murano, and F. Serra
Atomic force microscope characterization of a resonating nanocantilever
Ultramicroscopy, 2003. **97**(1-4): p. 127-133.

75. Liu, X., A. San Paulo, M. Park, and J. Bokor
Characterization of acoustic vibration modes at GHz frequencies in bulk acoustic wave resonators by combination of scanning laser interferometry and scanning acoustic force microscopy
in the proceedings of the *IEEE MEMS*. 2005.

76. San Paulo, A. and J. Bokor
Scanning acoustic force microscopy characterization of thermal expansion effects on the electromechanical properties of film bulk acoustic resonators
Applied Physics Letters, 2005. **86**(8).

77. Kobayashi, T., J. Tsaur, M. Ichiki, and R. Maeda
Fabrication and performance of a flat piezoelectric cantilever obtained using a sol-gel derived PZT thick film deposited on a SOI wafer
Smart Materials & Structures, 2006. **15**(1): p. S137-S140.

78. Li, Y.C., M.H. Ho, S.J. Hung, M.H. Chen, and M.S.C. Lu
CMOS micromachined capacitive cantilevers for mass sensing
Journal of Micromechanics and Microengineering, 2006. **16**(12): p. 2659-2665.

79. Abadal, G., Z.J. Davis, B. Helbo, X. Borrise, R. Ruiz, A. Boisen, F. Campabadal, J. Esteve, E. Figueras, F. Perez-Murano, and N. Barniol
Electromechanical model of a resonating nano-cantilever-based sensor for high-resolution and high-sensitivity mass detection
Nanotechnology, 2001. **12**(2): p. 100-104.

80. Davis, Z.J., G. Abadal, O. Kuhn, O. Hansen, F. Grey, and A. Boisen
Fabrication and characterization of nanoresonating devices for mass detection
Journal of Vacuum Science & Technology B, 2000. **18**(2): p. 612-616.

81. Li, M., H.X. Tang, and M.L. Roukes
Ultra-sensitive NEMS-based cantilevers for sensing, scanned probe and very high-frequency applications
Nature Nanotechnology, 2007. **2**(2): p. 114-120.

82. Villanueva, G., J. Montserrat, F. Perez-Murano, G. Rius, and J. Bausells
Submicron piezoresistive cantilevers in a CMOS-compatible technology for intermolecular force detection
Microelectronic Engineering, 2004. **73-74**: p. 480-486.

83. Narine, S.S., R. Hughes, and A.J. Slavin
The use of inductively coupled plasma mass spectrometry to provide an absolute measurement of surface coverage, and comparison with the quartz crystal microbalance
Applied Surface Science, 1999. **137**(1-4): p. 204-206.

84. Narine, S.S. and A.J. Slavin
Use of the quartz crystal microbalance to measure the mass of submonolayer deposits: Measuring the stoichiometry of surface oxides
Journal of Vacuum Science & Technology a-Vacuum Surfaces and Films, 1998. **16**(3): p. 1857-1862.

85. Ilic, B., H.G. Craighead, S. Krylov, W. Senaratne, C. Ober, and P. Neuzil
Attogram detection using nanoelectromechanical oscillators
Journal of Applied Physics, 2004. **95**(7): p. 3694-3703.

86. Verd, J., A. Uranga, J. Teva, G. Abadal, F. Torres, J. Arcamone, J.L. López, F. Pérez-Murano, J. Fraxedas, J. Esteve, and N. Barniol
Monolithic 0.35um CMOS cantilever for mass sensing in the attogram range with self-excitation
in the proceedings of the *IEEE Transducers*. 2007. Lyon, France.

87. Ilic, B., Y. Yang, and H.G. Craighead
Virus detection using nanoelectromechanical devices
Applied Physics Letters, 2004. **85**(13): p. 2604-2606.

88. Friedli, V., C. Santschi, J. Michler, P. Hoffmann, and I. Utke
Mass sensor for in situ monitoring of focused ion and electron beam induced processes
Applied Physics Letters, 2007. **90**(5).

89. Ramos, D., J. Tamayo, J. Mertens, M. Calleja, and A. Zaballos
Origin of the response of nanomechanical resonators to bacteria adsorption
Journal of Applied Physics, 2006. **100**(10).

90. Kim, S.J., T. Ono, and M. Esashi
Capacitive resonant mass sensor with frequency demodulation detection based on resonant circuit
Applied Physics Letters, 2006. **88**(5).

91. Vig, J.R. and Y. Kim
Noise in microelectromechanical system resonators
IEEE Transactions on Ultrasonics Ferroelectrics and Frequency Control, 1999. **46**(6): p. 1558-1565.

92. Dohn, S., O. Hansen, and A. Boisen
Cantilever based mass sensor with hard contact readout
Applied Physics Letters, 2006. **88**(26).

93. Spletzer, M., A. Raman, A.Q. Wu, X.F. Xu, and R. Reifenberger
Ultrasensitive mass sensing using mode localization in coupled microcantilevers
Applied Physics Letters, 2006. **88**(25).

94. Dohn, S., R. Sandberg, W. Svendsen, and A. Boisen
Enhanced functionality of cantilever based mass sensors using higher modes
Applied Physics Letters, 2005. **86**(23).

95. Sharos, L.B., A. Raman, S. Crittenden, and R. Reifenberger
Enhanced mass sensing using torsional and lateral resonances in microcantilevers
Applied Physics Letters, 2004. **84**(23): p. 4638-4640.

96. Tseytlin, Y.M.
High resonant mass sensor evaluation: An effective method
Review of Scientific Instruments, 2005. **76**(11).

97. Buks, E. and B. Yurke
Mass detection with a nonlinear nanomechanical resonator
Physical Review E, 2006. **74**(4).

98. Davis, Z.J. and A. Boisen
Aluminum nanocantilevers for high sensitivity mass sensors
Applied Physics Letters, 2005. **87**(1).

99. De Vlaminck, I., K. De Greve, L. Lagae, and G. Borghs
Silicon nanomechanical resonators with a double-triangle cross section leading to an enhanced mass sensitivity
Applied Physics Letters, 2006. **88**(6).

CHAPTER 2

CONCEPTS OF NANO/MICROMECHANICAL RESONATORS FOR MASS SENSING APPLICATIONS WITH ALL ELECTRIC ACTUATION AND DETECTION

I. Response of micro/nanomechanical resonators-based systems 34
I.1. Equations of oscillating systems 34
I.1.a. Harmonic (undamped non-driven) oscillators 34
I.1.b. Damped non-driven oscillators. 35
I.1.c. Driven damped oscillators 35
I.2. Resonance frequency of nano/micromechanical resonators: Analytical modeling 37
I.2.a. General equations 37
I.2.b. Cantilever and bridge 40
I.2.b.i) Cantilever 40
I.2.b.ii) Bridge 42
I.2.c. Quad-beams resonators 42
I.3. Mass sensitivity of nano/micromechanical resonators 48
I.3.a. Calculation of mass sensitivity 48
I.3.a.i) Punctual mass sensitivity 48
I.3.a.ii) Areal mass sensitivity 49
I.3.b. Dynamic linear range 50
II. Electrical response of electrostatically driven resonators 51
II.1. Transduction principle: capacitive detection with electrostatic actuation 51
II.2. Equivalent electrical modeling of a mechanical resonator 52
II.2.a. Global equivalent electrical scheme 52
II.2.b. RLC equivalent model of the motional impedance 54
II.2.b.i) Phenomenological approach of a RLC oscillator 54
II.2.b.ii) Parameters calculation 57
II.2.c. Global response 59
II.3. Response to electrostatic actuation 60
II.3.a. Deflection and pull-in voltage related to electrostatic force 60
II.3.b. Spring-softening effect 62

II.3.c. Generalization ... 63
III. Two approaches of flexural mode resonators: Out-of-plane and in-plane vibrating resonators ... 65
III.1. Out-of-plane flexion mode resonators ... 65
III.1.a. Comparison in terms of electrical response of three discrete devices with simplified RLC model ... 65
III.1.b. Comparison in terms of mass sensitivity (punctual and distributed) ... 67
III.1.b.i) Punctual mass sensitivity ... 67
III.1.b.ii) Distributed mass sensitivity ... 67
III.1.c. Analysis of the quad-beams device ... 68
III.1.c.i) Electromechanical modeling ... 68
III.1.c.ii) Fabrication of discrete devices: e-beam lithography on SOI ... 70
III.1.c.iii) Measurement of discrete devices ... 72
III.2. In-plane flexion mode resonators. Cantilevers ... 74
Conclusion of chapter 2 ... 76
Bibliographical references ... 77

The concept of measuring ultra-small masses using resonating micro and nanomechanical devices has been a subject of growing interest in the last few years [1-3]. The principle of operation is based on the detection of the shift of resonance frequency when a small quantity of mass is deposited on top of the mechanical structure. In general, the smaller the resonator, the more sensitive it is because the relative change of mass is greater. Compared to quartz crystal microbalances (QCM), micro and nanomechanical resonators may offer advantages in terms of sensitivity and system integration. In addition, if they are small enough, they can provide mass sensing with spatial resolution (concept of spatially localized detection).

For the readout of resonator oscillations, magnetomotive [3-5] and optical characterization techniques are the most cited in the literature. The first requires a heavy set-up while the second offers very high resolution under various configurations (through interferometric technique [6, 7] or with atomic force microscopy (AFM) based set-ups). However, with the aim of conceiving a portable and non-invasive system, our research has been focused on a purely electric actuation and detection method. The reasons of this choice and the features of this technique will be exposed later in this chapter.

In relation with this aspect, this thesis has been focused on the study of silicon based micro and nanomechanical devices since they can be fabricated in batch using standard silicon technology process and they can be combined with CMOS technology to fabricate monolithic integrated microsystems. It allows the assembly of arrays and matrices of resonators [8, 9], and the development of portable systems with integrated read-out circuitry for signal processing and conditioning. With regard to this matter, the monolithic integration of nano/micromechanical resonators [10, 11] is precisely the topic of chapters 3, 4 and 5.

In this chapter, the basic physical concepts related to the application of silicon nano/micromechanical resonators as ultra-sensitive mass sensors will be tackled. First, the prediction of their mechanical frequency response will be studied.

Second, their electrical response to electrostatic actuation will be analyzed: in particular the issue of converting a mechanical motion into an electrical signal with a capacitive readout scheme will be addressed. Then it will be explained how to model such a mechanical component like an electrical element. This will help in predicting the resonance signal level and open up possibilities of performing SPICE-type simulations for the study of the coupled system resonator/CMOS circuit. Then, the influence of the excitation signal upon the mechanical frequency response will be analyzed.

Third, two ways of operating micromechanical resonators will be studied: in their out-of-plane and in their in-plane flexural mode. Both modes of operation have well distinct features and these will be compared in terms of electrical and sensing performances.

I. Response of micro/nanomechanical resonators-based systems

This section describes the general behavior of a mechanical oscillator. We will consider in detail the calculation of the mechanical resonance frequency for three specific shapes:

- cantilevers, i.e. singly clamped beams (only anchored at one end)
- bridges, i.e. doubly clamped beams
- quad-beams (QB), that consist of a central plate with four beams

Finally, the basic modeling for obtaining the mechanical mass sensitivity will be developed.

I.1. Equations of oscillating systems

The description of a mechanical resonator as a harmonic oscillator is useful to catch the main features of a resonant structure. In this sense, the simplest way to model a mechanical resonator is the mass-spring system (Figure 1):

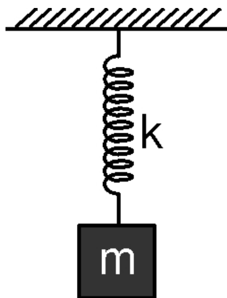

Figure 1. Mass spring system

m is the dynamic (or effective) mass of the system, *k* is the spring constant (or stiffness). Both depend on the vibration mode and on the characteristics of the applied force (uniformly or punctually applied, and at which point). By solving the equation of motion, the resonance frequency can be addressed.

In the following section, three general configurations of force balances are tackled.

I.1.a. Harmonic (undamped non-driven) oscillators.

In a first and simplified approach, the oscillator is considered purely harmonic, what means that (i) the damping of the medium in which dynamic motion occurs is not considered and that (ii) no external force drives it. Then, only the spring force acting in the opposite direction of the spring stretching intervenes. It is proportional to the displacement x and the stiffness k. The balance is:

$$F = -kx = m\frac{d^2x}{dt^2} \tag{II.1}$$

a general solution is $x = A\sin(\omega t + \varphi)$. From eq.(II.1), we deduce:

$$\omega_0 = 2\pi f_0 = \sqrt{\frac{k}{m}} \tag{II.2}$$

where ω_0 is the natural angular resonance frequency, and f_0 the natural resonance frequency also named eigenfrequency.

I.1.b. Damped non-driven oscillators.

Let us consider now a damping force acting on the resonator and arising from the surrounding medium (air, liquid, etc…). The damping is modeled as a force proportional to the displacement velocity that acts in the opposite direction of the bending. Compared to eq.(II.1), one additional term must be included in the force balance:

$$-kx - D\frac{dx}{dt} = m\frac{d^2x}{dt^2} \tag{II.3}$$

D is called coefficient of damping force. Rewriting eq.(II.3) and given $\omega_0^2 = \frac{k}{m}$, then:

$$\ddot{x} + 2n\dot{x} + \frac{k}{m}x = 0 \text{ with } n = \frac{D}{2m} \tag{II.4}$$

The solutions of this homogeneous differential equation are given by $\lambda^2 + 2n\lambda + \omega_0^2 = 0$. This results in:

$$\lambda_{1,2} = -n \pm \sqrt{n^2 - \omega_0^2} \tag{II.5}$$

The response of the system can be discussed according to the ratio $\xi = \frac{n}{\omega_0}$:

- case of slight damping, $n < \omega_0$, then $\lambda_{1,2} = -n \pm i\sqrt{\omega_0^2 - n^2}$. One solution is:

$$x = Ae^{-nt}\sin\left(\sqrt{\omega_0^2 - n^2}\,t + \alpha\right) = Ae^{-nt}\sin\left(\omega_D t + \alpha\right) \tag{II.6}$$

with
$$\omega_D = \sqrt{\omega_0^2 - n^2} = \omega_0\sqrt{1-\xi^2} \tag{II.7}$$

  This means that the system oscillates at a certain angular frequency with a time decreasing amplitude (first term of the solution).

  ω_D is the angular resonance frequency of the oscillator in presence of slight damping, it differs from pure resonance towards lower values depending on the magnitude of the damping coefficient n. In practice, in air, ω_0 and ω_D differ very few.

- for critical damping and heavy damping ($n \geq \omega_0$), no oscillations occur, only a limited displacement returning to stationary position.

I.1.c. Driven damped oscillators

In practice, mechanical systems are always confronted to damping arising from both the surrounding medium and internal energy losses (c.f. chapter 1).

This requires a permanent external solicitation to provide energy in order to maintain the oscillations; this is the so-called forced regime in which a periodic external force is applied. Let us formulate again the balance with a sinusoidal external excitation:

$$m\frac{d^2x}{dt^2}+c\frac{dx}{dt}+kx=F_{exc}(t)=F_0\sin(\omega t) \tag{II.8}$$

A solution is $x=x_1+x_2$, where x_1 is the solution of the homogeneous differential equation like eq.(II.6). For x_2 we assume: $x_2=W_2\sin(\omega t-\varphi)$. Setting $A=\frac{F_0}{m}$, so:

$$W_2=\frac{A}{\sqrt{\left(\omega_0^{\,2}-\omega^2\right)^2+4n^2\omega^2}} \quad \text{and} \quad \varphi=\arctan\frac{2n\omega}{\omega_0^{\,2}-\omega^2} \tag{II.9}$$

Transient oscillations arising from x_1 are disregarded; only the steady solution x_2 is considered. The frequency of the steady vibration is the same as the one of the driving force, but there is a phase lag φ (function of free vibration frequency f_0, driving force F_0 and damping coefficient n). According to eq.(II.9), there is a 180° phase change around f_0. From the expression of W_2, the Q-factor can be theoretically estimated as:

$$Q\approx\frac{1}{2\xi}=\frac{\omega_0}{2n} \tag{II.10}$$

The resonance frequency f_r corresponds to a maximum in amplitude, in other words when W_2 is maximized. It is actually shifted downward with respect to f_0 according to:

$$f_r=f_0\sqrt{1-2\xi^2} \tag{II.11}$$

From eq.(II.11), we learn that, theoretically, if $\xi\geq 0.7$, the peak would disappear.

As an example, the amplitude-frequency response given by eq.(II.9) is plotted for A=1, ω_0=1, and n=0.05, 0.125, 0.25, 0.375 and 0.5. It is clear from this graph that the higher is n, the lower are the peak magnitude and the quality factor (see eq.(II.10)). Furthermore, the resonance frequency is clearly shifted down to lower values when n increases:

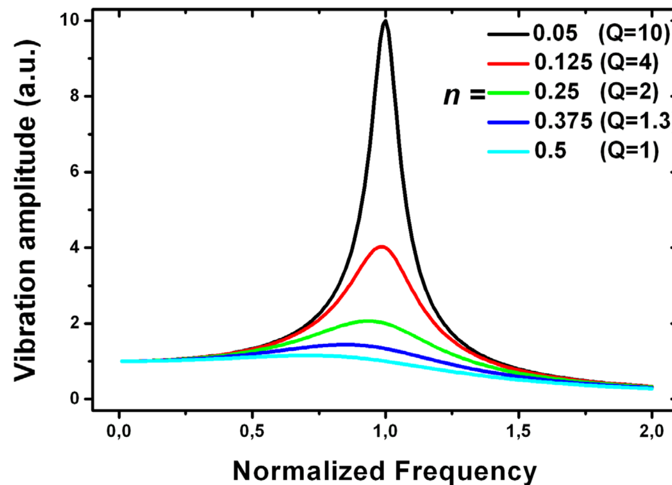

Figure 2. Amplitude-frequency response normalized to a frequency of 1 for several n factors

As a conclusion, and after validation of this observation based on experimental results, in practice our resonators (operated either in air or vacuum) are always in the case of slight damping, and thereby f_0, f_D and f_r are very close to each other. Indeed, Q-factors of at least 10 have always been observed: according to eq.(II.10), this corresponds to $\xi = 0.05$. Consequently, the resonance frequency of the driven damped resonator is $f_r = 0.997 f_0$ following eq.(II.11).

A practical consequence of this is that if we wish to theoretically predict the resonance frequency of nano/micromechanical devices, in first approximation the effects of driving and damping do not need to be taken in account.

I.2. Resonance frequency of nano/micromechanical resonators: Analytical modeling

This section deals with mechanics of nano/micromechanical elements and, in particular, with methods allowing the determination of the resonance frequency. An analytical approach is followed trying to find out direct methods for three different resonator shapes: cantilever, bridge and quad-beams. The analytical study of most practical problems give good enough results for design optimization, as in most cases the performances of mechanical sensors are more significantly affected by process variations than by analytical approximations.

Our samples have dimensions in the micron and submicron scale (typically between 200 nm and 20 µm), but still equations of macroscopic elastic continuum mechanics are employed. The experimental results will further justify this approach since these laws still seem to predict relatively accurately the resonance frequency at these scales, in other words no mechanical effect specifically related to the nanoscale has been significantly observed.

I.2.a. General equations

EULER-BERNOUILLI EQUATION

This approach [12] is also called method of differential equations. This is a fundamental method for finding the vibration frequencies and the shape functions of all the vibration modes. In principle, it can be applicable to any structure but very often numerical methods are needed due to the complexity of the calculation. Here, the study is restricted to the relatively simple case of beam structures.

The free vibration of a beam at small amplitude can be described by a partial differential equation. According to section I.1, the calculation can be simplified neglecting the damping and driving forces. Then, making a balance of forces on an element section of a beam (provided the ratio length/thickness is much larger than 1) and neglecting its own loading (gravitational force), the Newton's law can be written under the form [12]:

$$\rho_m A \frac{\partial^2 w}{\partial t^2} + E\,I \frac{\partial^4 w}{\partial x^4} = 0 \tag{II.12}$$

where A is the cross-section area, w is the displacement in the direction of vibration, x is the cantilever length axis, t is the time, ρ_m is the cantilever material density, E is the Young modulus

(according to elastic Hooke's law). I is the moment of inertia of the beam for out-of-plane motions and is given by:

$$I = \int_{-h/2}^{h/2} z^2 b(z) dz = \frac{b\,h^3}{12} \tag{II.13}$$

where b and h are respectively the beam width and thickness

A general solution is a linear combination of each mode of vibration:

$$w(x,t) = \sum_{i=o}^{n} C_i \sin(\omega_i t + \varphi_i)\phi_i(x) \tag{II.14}$$

where ω_i is the resonance frequency and ϕ_i the shape of the ith mode.

Thus, eq.(II.12) can be reduced to $\frac{\partial^4 \phi_i}{\partial x^4} = -\frac{\rho_m A \omega_i^2}{EI}\phi_i$ of which a solution is:

$$\phi_i(x) = a_i \cos\left(\frac{x}{\kappa_i}\right) + b_i \cosh\left(\frac{x}{\kappa_i}\right) + c_i \sin\left(\frac{x}{\kappa_i}\right) + d_i \sinh\left(\frac{x}{\kappa_i}\right) \tag{II.15}$$

where $\kappa_i = \sqrt[4]{\frac{EI}{\rho_m A \omega_i^2}}$

Then, depending on the considered structure (singly, doubly clamped, etc...), specific boundary conditions must be applied to ϕ_i so that the detailed expression of ω_i can be extracted.

RAYLEIGH-RITZ METHOD [12]

In this method also, the mechanical properties of silicon nano and microstructures are assumed to be ideally elastic and homogeneous. In these conditions, the vibration frequency of a specific mode can be determined if the shape function of this mode is known. The problem is that in general it is not straightforward to foresee the shape functions of complex structures. However, the vibration frequency of the fundamental mode (i.e. with the lowest resonance frequency) whose shape function is generally known, can be found with high accuracy (however the result provided by this method will always be only an approximation of the real eigenfrequency).

The strategy to follow is to find first the shape function w(x). For this purpose, the total bending moment M(x) acting on the beam is expressed. This is a classical approach in mechanics that consists in calculating the integral of the moment of forces across the cross section of the beam. This expression can be put under the form [12]:

$$M(x) = \int z\,dF = -E\,I\,w''(x) \tag{II.16}$$

where x is the cantilever length axis, E is the Young modulus, I the moment of inertia of the beam and $w''(x)$ is the second derivative of the shape function with respect to x.

Eq. (II.16) can be applied to any specific beam-like structure adapting the left part [M(x)] of the equation by making the adequate balance of the moments and applying the specific boundary conditions. Hence, $w''(x)$ must be twice integrated so that $w(x)$ (the so-called shape function) is finally determined.

The total potential energy (related to the bending) and kinetic energy of the whole beam are respectively [12]:

$$E_P = \frac{1}{2}\int_0^l E\,I(x)\,w''^2(x,t)\,dx \tag{II.17}$$

$$E_K = \frac{1}{2}\int_0^l \rho\,b(x)\,h(x)\left(\frac{dw}{dt}\right)^2 dx \tag{II.18}$$

where $b(x)$, $h(x)$ and l are the beam width, thickness and length respectively (x is still axis in the direction of the length). In general, the vibration of a beam structure can be described by:

$$w(x,t) = \sum_{n=0}^{\infty} c_n\, w_n(x,t) = \sum_{n=0}^{\infty} c_n\left[w_n(x)\sin(\omega_n t + \varphi_n)\right] \tag{II.19}$$

where $w_n(x,t)$ indicates a specific vibration mode (with specific coefficient c_n) corresponding to a sinusoidal vibration of frequency ω_n and whose shape function is $w_n(x)$. Mathematically, $w_n(x,t)$ are the eigenfunctions of the vibration system.

Computing eq. (II.17) and (II.18) with eq.(II.19), the potential and kinetic energy can be expressed for each mode thus containing a time-varying sinusoidal component:

$$E_P = \frac{1}{2}c_n^2\int_0^l E\,I(x)\,w_n''^2(x)\sin^2(\omega_n t + \varphi_n)\,dx \quad and \quad E_P = \int_0^l \rho\,b(x)\,h(x)\,w_n^2(x)\,\omega_n^2\cos^2(\omega_n t + \varphi_n)\,dx \tag{II.20}$$

According to the principle of energy conservation (E_{Pmax}=E_{Kmax}=E), both maximum are equal:

$$E_{P\max} = \frac{1}{2}c_n^2\int_0^l E\,I(x)\,w_n''^2(x)\,dx = E_{K\max} = \frac{1}{2}c_n^2\int_0^l \rho\,b(x)\,h(x)\,w_n^2(x)\,\omega_n^2\,dx \tag{II.21}$$

From that, the angular resonance frequency contained in the term of kinetic energy can be extracted to define the so-called Rayleigh-Ritz quotient [12] that provides the radial resonance ω_n frequency for any vibration mode:

$$\omega_n^2 = \frac{\int_0^l E\,I(x)\,w_n''^2(x)\,dx}{\int_0^l \rho\,b(x)\,h(x)\,w_n^2(x)\,dx} \tag{II.22}$$

I.2.b. Cantilever and bridge

I.2.b.i) Cantilever

Beams clamped in one side only are named cantilevers. This is the simplest resonator design.

In this section, the cantilever dimension in the direction of vibration will be named *h*.

Following the Euler-Bernouilli approach, the following boundary conditions are applied to eq.(II.15):

$$\phi_1(0) = 0 \text{ , } \phi_1'(0) = 0 \text{ and } \phi_1''(l) = 0$$

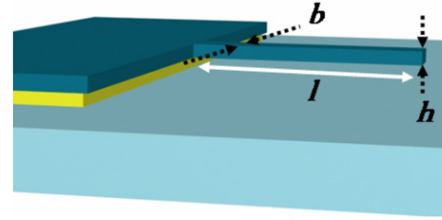

Figure 3. Cantilever resonator. *l*, *h* and *b* are its length, thickness and width respectively

what results in:

$$\omega_1 = 1.015\sqrt{\frac{E}{\rho_m}}\frac{h}{l^2} \text{ and } \omega_2 = 6.361\sqrt{\frac{E}{\rho_m}}\frac{h}{l^2} \tag{II.23}$$

and more generally

$$\omega_n = \sqrt{\frac{(2n-1)^4\pi^4}{192}}\sqrt{\frac{E}{\rho_m}}\frac{h}{l^2} = \psi_n\sqrt{\frac{E}{\rho_m}}\frac{h}{l^2} \text{ [13]} \tag{II.24}$$

where ψ_n is a constant depending on the vibration mode.

A second approach, more convenient to subsequently estimate the mass sensitivity of the device, is to rely on the equation of a mass-spring system (eq.(II.2)): $\omega_n = \sqrt{\frac{k_n}{m_{EFF_n}}}$, what implies the separate determination for a given mode n of (i) the cantilever stiffness k_n, and (ii) its effective mass m_{EFF_n}. Nevertheless, in the case of a cantilever, this formula must be manipulated with caution since the mass is not located in one single point at the extremity, like in the mass-spring model originating this formula, but uniformly distributed. Consequently a corrective term α_{1_n} must be applied to *m* in order to obtain the efficient mass m_{EFF_n} :

$$m_{EFF_n} = \alpha_{1_n} m = \alpha_{1_n} lbh \tag{II.25}$$

Regarding the stiffness k_n, it depends on the point of application of the force and on its distribution upon the cantilever. Another corrective term α_{2_n} needs to be applied:

$$k_n = \alpha_{2_n}\frac{Eh^3b}{l^3} \tag{II.26}$$

Books of Mechanics (for example [12]) generally provide the value of α_{2_n} in general cases. Considering eq.(II.24), it comes that α_{1_n} can be deduced from α_{2_n} through the relation:

$$\alpha_{1_n} = \frac{\alpha_{2_n}}{\psi_n^{\,2}} \tag{II.27}$$

Table II - 1 reports α coefficients for the fundamental flexural mode (here, out-of-plane) in two common cases:

	α_1	α_2
Punctual force applied at the free end	0.243	0.25
Distributed force uniformly applied on the cantilever	0.647	$\frac{2}{3}$

Table II - 1. α coefficients of a cantilever for two different force loadings

A third approach consists in employing the Rayleigh-Ritz method. Relying on the balance of bending moments, it becomes relatively easy to evaluate the resonance frequency of a cantilever with and without a mass at the free end. Following the strategy previously exposed, the shape function of a cantilever under an uniform load F_U of any nature is given by [12]:

$$\boldsymbol{w(x)} = \frac{\boldsymbol{F_U}}{2\boldsymbol{E\,b\,l\,h}^3}\boldsymbol{x}^2\left(\boldsymbol{x}^2 - 4\boldsymbol{l\,x} + 6\boldsymbol{l}^2\right) \tag{II.28}$$

what results in the following expression after making the Rayleigh-Ritz quotient (eq.(II.22)):

$$\omega_1 = 1.019\sqrt{\frac{\boldsymbol{E}}{\rho_m}}\frac{\boldsymbol{h}}{\boldsymbol{l}^2} \tag{II.29}$$

Comparing with eq.(II.23), one can notice that the value provided by this method is slightly higher but extremely close to it (ψ_1 =1.019 with this method instead of 1.015).

Following again the strategy previously exposed, we try to calculate the resonance frequency of a cantilever loaded at its free end with a punctual force F_P (for example with a mass much larger than its own mass). First, the shape function is estimated through a balance of moments without taking into account the mass of the beam, so that the shape expression is much simplified [12]:

$$\boldsymbol{w(x)} = \frac{2\boldsymbol{F_P}}{\boldsymbol{E\,b\,h}^3}\boldsymbol{x}^2\left(3\boldsymbol{l} - \boldsymbol{x}\right) \tag{II.30}$$

Then, the Rayleigh-Ritz quotient (eq.(II.22)) is calculated including also the beam mass (by integrating it along its length) in the term of kinetic energy what gives:

$$\omega_1 = \sqrt{\frac{\boldsymbol{E\,b\,h}^3}{4\left(\boldsymbol{M} + \frac{33}{140}\boldsymbol{M_b}\right)\boldsymbol{L}^3}} \equiv \sqrt{\frac{\boldsymbol{k_{BEAM}}}{\boldsymbol{m_{TOTAL}}}} \tag{II.31}$$

where M_b is the beam mass, M the mass located at the free end, $\boldsymbol{k_{BEAM}} = \frac{\boldsymbol{E\,b\,h}^3}{4\boldsymbol{L}^3}$ and $\boldsymbol{m_{TOTAL}} = \boldsymbol{M} + \frac{33}{140}\boldsymbol{M_b}$. k_{BEAM} corresponds to the stiffness for a punctual force applied at the free

end (α_2=0.25); while m_{TOTAL} expresses the equivalent mass of the beam in a mass-spring model. If M=0, then it comes that:

$\omega_1 = 1.03\sqrt{\frac{E}{\rho_m}}\frac{h}{l^2}$, not differing much from eq. (II.23)

This demonstrates that the Rayleigh Ritz quotient is sufficiently accurate even with approximated shape functions.

I.2.b.ii) Bridge

The doubly clamped beam, also named bridge, is rigidly anchored at its two extremities.

In this section, the bridge dimension in the direction of vibration will be named h.

Following the Euler-Bernouilli approach, the following boundary conditions are applied to eq.(II.15):

$$\phi_1(0) = \phi_1(l) = 0\ ,\ \phi_1{}'(0) = \phi_1{}'(l) = \phi_1{}'(\frac{l}{2}) = 0$$

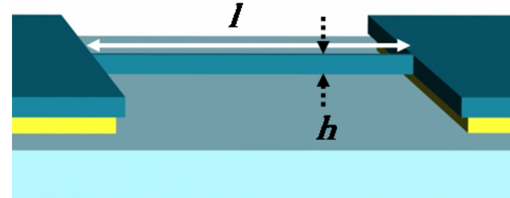

Figure 4. Bridge resonator. l and h are its length and thickness respectively. b, not depicted here, is the bridge width.

Following the second approach of previous section whereby the angular resonance frequency is estimated basing on the mass-spring model, α coefficients and angular resonance frequency are reported in Table II - 2 for the fundamental out-of-plane flexural mode in two common cases:

	α_1	α_2	ω_1
Punctual force applied at the mid-point	0.379	16	$6.5\sqrt{\frac{E}{\rho_m}}\frac{h}{l^2}$
Distributed force uniformly applied on the cantilever	0.757	32	

Table II - 2. α coefficients of a bridge for two different force loadings

I.2.c. Quad-beams resonators

A quad-beam (QB) resonator is formed by a central plate and four (doubly clamped) beams (Figure 5).

This configuration is a nice example of structure intrinsically equivalent to a spring-mass system in the sense that both elements are well dissociated: on one part four beams acting like a spring of negligible mass, and on another a plate, that does not deform, acting as a mass.

By shrinking the dimensions of the beams down to the micron/submicron range, resonance frequencies in the MHz can be attained for the out-of-plane flexural fundamental mode while maintaining the central plate area relatively large.

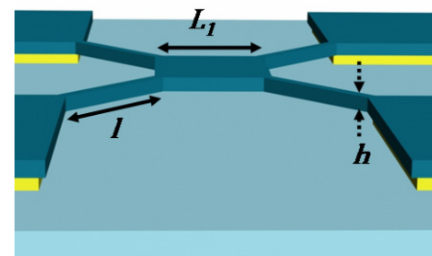

Figure 5. Quad beam resonator with a central square plate of width L_1, and four beams of length and thickness of l and h respectively. b, not depicted here, is the width of the beams.

This large area is an advantage regarding the capacitive coupling with the substrate (as it will be detailed in section II, the technique of resonance detection we employ is capacitive).

Concerning the further objective of implementing the device as a mass sensor (depositing mass on the central plate), the QB is adequate for the following reasons:

- mechanically speaking, it remains relatively insensitive both to the adsorbate stiffness (which ensures the mass loading effect is mechanically dominant [14-16]) and to the adsorbate position within the central plate. On the opposite, a cantilever is very sensitive to the location of the adsorbate [17].
- the large area of the central plate makes more convenient the deposition of particles or the dispensing of liquid for their mass measurement.

In order to find out the most accurate way to predict the resonance frequency, a comparison between several approaches is undertaken, all based on more or less refined Rayleigh-Ritz methods. Methods 1, 2 and 3 are the most simple (the effect caused by the underetching of the anchors is neglected), although methods 4 and 5 are more complex as they do take into account the effect of the underetching of the anchors and the own mass of the beams.

According to Figure 5, the following dimensions are defined: L_1 as plate width (square shaped plate), l as beam length, b as beam width, h as structural layer thickness. E is the Young modulus, ρ the polysilicon density (structural material), ω the angular frequency, m the plate mass $\left(=\rho L_1^2 h\right)$ and m_b the mass of one single beam $\left(=\rho l w h\right)$. Quad-beams with diagonal beams (like in Figure 5) and with parallel beams have been analyzed. In methods 1, 2 and 3, these two configurations do not require separate calculations. On the contrary, when considering the effect of the underetching of the anchors, like in methods 4 and 5, both cases must be dissociated.

Method 1 The Rayleigh-Ritz method is applied to an anchored beam with final mass $m/4$ (one quarter of the central plate mass). The own mass of the beams is neglected and the effect caused by the underetching of the anchors as well. Making a balance of the bending moments, a punctual force F_P is considered at the end of each beam (on the side of the central plate):

$$M(x) = -EIw''(x) = F_P\, x - M_0 \qquad \text{(II.32)}$$

where M_0 is a restrictive moment to be determined. Here $w(0)=w'(0)=0$, $w'(l)=0$ and $w''(l/2)=0$, so $M_0 = \frac{1}{2} F_P\, l$ and $EIw''(x) = F_P\left(\frac{l}{2} - x\right)$, so $w''(x) = \frac{12\, F_P}{E\, b\, h^3}(l/2 - x)$. After a double integration, the shape function is obtained:

$$w(x) = \frac{F_P}{E\, b\, h^3}\left(\frac{l x^2}{4} - \frac{x^3}{3}\right) \qquad \text{(II.33)}$$

The Rayleigh-Ritz quotient is applied to this shape function. In the term of kinetic energy, we only consider the punctual mass $m/4$ located at the beam end ($x = l$):

$$\omega_1^2 = \frac{\int_0^l E\, I(x) w''^2(x) dx}{\frac{1}{4} m\, w^2(l)} \quad \text{(II.34)}$$

what results in:

$$\omega_1 = \sqrt{\frac{4 E b\, h^3}{m l^3}} \text{, equivalent to } \omega_1 = 2\sqrt{\frac{E}{\rho_m} \frac{h\, b^{0.5}}{L_1\, l^{1.5}}} \quad \text{(II.35)}$$

Method 2 Eq.(II.31) is taken as a basis. This corresponds to the case of a cantilever beam: (i) loaded with a punctual mass located at its moving end and (ii) whose own mass is also taken into account. However here, the total spring constant is assumed to be equal to four times the one of a single beam:

$$\omega_1 = \sqrt{4\left(\frac{E\, b\, h^3}{4 l^3}\right) \frac{1}{\left(m + \frac{33}{140} m_b\right)}} = \sqrt{\frac{E\, b\, h^3}{\left(m + \frac{33}{140} m_b\right) l^3}} \quad \text{(II.36)}$$

Method 3 A similar approach to method 2 is followed, but considering a spring constant of one single beam that is loaded at its moving end with a punctual mass *m*/4.

$$\omega_1 = \sqrt{\frac{E\, b\, h^3}{4 l^3} \frac{1}{\left(\left[\frac{m}{4}\right] + \frac{33}{140} m_b\right)}} = \sqrt{\frac{E\, b\, h^3}{\left(m + \frac{132}{140} m_b\right) l^3}} \quad \text{(II.37)}$$

In practice, the results provided by methods 2 and 3 are very close since the beam mass is rather small compared to the plate mass.

Now, more exhaustive methods are going to be detailed. The related calculations have required the use of the *Mathematica* software (www.wolfram.com) and the resulting analytical expressions are so long and complex that they are not provided in this manuscript. Hereafter, we describe and insist on the guidelines of these calculations.

Method 4 In this method, the aim is to calculate the resonance frequency of diagonal or parallel quad-beams taking into account the effect caused by the underetching of the anchors but neglecting the mass of the four beams.

The anchor underetching arises from the wet etching performed to release the central plate. In Figure 6, a quad-beam (fabricated at CNM in the framework of this thesis) is depicted. It has been successfully released but the counter consequence is that the anchors of the four beams are also underetched over a distance *S* since the etching is isotropic. In first approximation, this extension *S* is equivalent to the half-width of the plate:

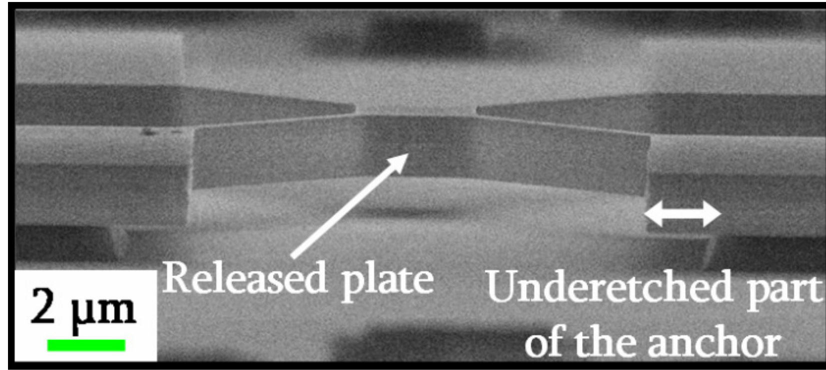

Figure 6. SEM image of a Si quad-beam with underetched anchors

DIAGONAL QUAD-BEAMS

The first step is to make the balance of bending moments:

$$M(x) = -E\,I\,w''(x) = F_P\,x - M_0 \tag{II.38}$$

The boundary conditions are: $w(0)=w'(0)=0$, $w'(l)=0$. However here, $w''(l/2)=0$ is not true since the exact location of the inflexion point is not known (the symmetry is modified by the underetching extension). Consequently, M_0 cannot be directly determined.

In the Rayleigh-Ritz method, it is necessary to predict the shape function $w(x)$ of the movable part. Figure 7 depicts the part that is bent:

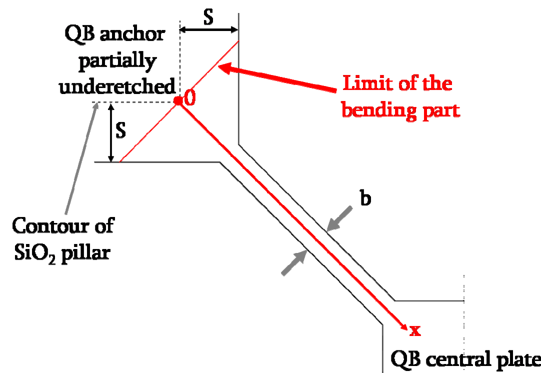

Figure 7. Schematic partial top-view of a QB whose anchor is affected by underetching

This modifies the calculation of the moment of inertia. For out-of-plane vibrations, $I = \int_{-h/2}^{h/2} z^2 b(x,z)dz = \frac{b(x)h^3}{12}$ but here specifically, b is not constant and depends on x. Introducing this expression into eq.(II.38), the second derivative of the shape function can be expressed as:

$$w''(x) = \frac{12\,M_0 - 12\,F_P\,x}{E\,b(x)\,h^3}$$

with the following conditions:

for x ∈ $\left[0;\sqrt{2}S-\frac{b}{2}\right]$, $b(x)=2\sqrt{2}S-2x$ resulting in $w_1''(x)=\frac{12\,M_0-12\,F_P\,x}{E\left(2\sqrt{2}S-2x\right)h^3}$ (II.39)

for x ∈ $\left[\sqrt{2}S-\frac{b}{2};l+\sqrt{2}S-\frac{b}{2}\right]$, $b(x)=b$ resulting in $w_2''(x)=\frac{12\,M_0-12\,F_P\,x}{E\,b\,h^3}$ (II.40)

PARALLEL QUAD-BEAMS

For parallel QB, the balance of bending moments is identical but here the movable part is totally different. What potentially moves is the whole anchor width. Intuitively, the effect of the underetching is lessened compared to the case of diagonal beams because the movable part of the anchor is much wider and therefore much stiffer.

The shape function to consider here is: $w''(x)=\frac{12\,M_0-12\,F_P\,x}{E\,b(x)\,h^3}$ with the following conditions:

for x ∈ $[0;S]$, $b(x)=P$ resulting in $w_1''(x)=\frac{12\,M_0-12\,F_P\,x}{E\,P\,h^3}$ (II.41)

for x ∈ $[S;l+S]$, $b(x)=b$ resulting in $w_2''(x)=\frac{12\,M_0-12\,F_P\,x}{E\,b\,h^3}$ (II.42)

where P is the width of the anchor.

DETERMINATION OF THE RESONANCE FREQUENCY FOR PARALLEL AND DIAGONAL QB:

Starting from the second derivative of the shape functions (eq.(II.39) and (II.40), or (II.41) and (II.42)), we integrate them a first time according to $w_1'(0)=0$ and $w_2'(l)=0$. At this stage, the first derivatives (w_1' and w_2') are equaled at their junction point (x= $\sqrt{2}S-\frac{b}{2}$ for the diagonal ones, and x=S for the parallel ones) what also allows determining M_0. Then, w_1' and w_2' are integrated according to $w_1(0)=0$ and equaling w_1 and w_2 at their junction point. When making the Rayleigh-Ritz quotient, the term of kinetic energy is calculated considering a punctual mass (m/4) only located at the moving extremity of the beam (i.e. where it is anchored to the central plate).

Method 5 In this method, the aim is to calculate the resonance frequency of diagonal or parallel quad-beams taking into account both the effect caused by the underetching of the anchors and the mass of the beams.

Knowing that the Rayleigh-Ritz method is not very sensitive to the shape function and in order to simplify the balance of bending moments, that becomes very complex when considering the mass of the beam, the shape function is approximated with the one of methods 4. Then, the kinetic term of the Rayleigh-Ritz quotient is calculated integrating the mass all over the length of the moving part plus the punctual mass (m/4) located at the end of the beam.

The results of all the methods are reported in Table II - 3 and Table II - 4, in which experimental data of real devices (fabricated and measured according to techniques explained in forthcoming sections) are listed. Among these seven devices, six are diagonal and one is parallel while four have a monocrystalline silicon structural layer and three a polycrystalline one:

Device	E (GPa)	L_1 (µm)	l (µm)	b (nm)	h (µm)	S (µm)	f_0 (exp) (MHz)
Diag1 (single-crystal Si)	160	14	17.5	660	1.48	8	**1.72**
Diag2 (single-crystal Si)	160	14.6	22	700	1.47	9.5	**1.38**
Diag3 (single-crystal Si)	160	11.4	19.2	1050	1.47	9.5	**2.20**
Diag4 (single-crystal Si)	160	9.4	19.6	670	1.45	5.9	**2.58**
Diag5 (polySi)	130	6.25	13.45	765	450	3.5	**1.45**
Diag6 (polySi)	130	6.25	13.45	765	450	3.5	**1.49**
Par7 (polySi)	130	6.2	19.4	685	450	4	**1.23**

Table II - 3. Experimental characteristics of real devices and measured resonance frequency

Device	f_0 (M1) (MHz)	f_0 (M2) (MHz)	f_0 (M3) (MHz)	f_0 (exp) (MHz)	f_0 (M4) (MHz)	f_0 (M5) (MHz)	4 * m_{BEAM}/ m_{PLATE} (%)
Diag1 (single-crystal Si)	3.09	1.54	1.51	**1.72**	2.67	2.54	24
Diag2 (single-crystal Si)	2.15	1.07	1.04	**1.38**	1.9	1.79	29
Diag3 (single-crystal Si)	4.14	2.03	1.93	**2.20**	3.4	3.01	50
Diag4 (single-crystal Si)	3.84	1.89	1.80	**2.58**	3.46	3.1	59
Diag5 (polySi) Diag6 (polySi)	3.03	1.47	1.36	**1.45** **1.49**	2.66	2.22	105
Par7 (polySi)	1.67	0.8	0.72	**1.23**	1.65	1.34	138

Table II - 4. Comparison between theoretical (for the five methods) and experimental resonance frequency of real devices. The last column indicates the proportion of the mass of the beams respect to the plate mass

DISCUSSION OF THE RESULTS

The first remark to do is the major uncertainty in the determination of the devices parameters. Regarding the Young modulus, the one of monocrystalline Si depends upon the crystallographic orientation and can vary from 170 to 130 GPa whereas here a fixed value of 160 GPa has been considered. Concerning the polycrystalline structures, their Young modulus is not precisely known neither as it depends upon the deposition parameters.

Regarding the dimensions, it has been assumed in the models that all the four beams have identical dimensions and a rectangular shape. In practice it is not completely the case what complicates much the study. It has not been easy neither to measure the underetching affecting each device and additionally some dispersion in the thicknesses has been noticed although it has not been possible to check it for each device.

Second, another important uncertainty comes from the experimental value of the natural resonance frequency. It is estimated from a fit (of the curve that plots the resonance frequency as a function of the excitation voltage, c.f. section II.3.b). Experimentally, the curve is not always as linear as it should theoretically be.

Methods 2 and 3 seem to be the most accurate. In monocrystalline structures, theoretical values are smaller than experimental ones: one the reason for this may be that the Young modulus is underestimated. In polycrystalline structures, theoretical values are also smaller than experimental ones but probably because of the internal stress (some curvature has been observed).

I.3. Mass sensitivity of nano/micromechanical resonators

Regarding our aim of performing mass sensing experiments with nano/micromechanical resonators, methods to evaluate their mass sensitivity *S* are required. An usual and convenient way to determine the mass sensitivity of a given vibration mode is to start from the expression of the resonance frequency (of this mode) put under the form of the mass-spring system approach:

$$f = \frac{1}{2\pi}\sqrt{\frac{k_{EFF}}{m_{EFF}}} = \frac{1}{2\pi}\sqrt{\frac{k_{EFF}}{\alpha_1 m_{RES}}} \tag{II.43}$$

where k_{EFF}, m_{EFF} and m_{RES} are respectively the effective spring constant, effective mass and the resonator mass ($\alpha_1 = m_{EFF} / m_{RES}$ has been previously defined) of a given mode.

I.3.a. Calculation of mass sensitivity

For the determination of the mass sensitivity, our approach is based on the previous equation. In chapter 1, a survey of existing NEMS-based mass sensors has been proposed and it has been stated that depositing some mass on top of the resonator results in a resonance frequency shift that is a combination of three phenomena: (i) a mass loading leading to a frequency decrease (c.f. eq.(II.43) as the denominator increases), but also (ii) a stiffening effect caused by the additional contribution of the adsorbate and (iii) an adsorption-induced surface stress. Effects (ii) and (iii) both tend to increase the frequency (as the numerator of eq.(II.43) is increased). Here, the study is restricted to the case of very small mass accretions and to the deposition of low-stiffness low-stress materials (like liquids). Therefore, we will assume that the spring constant is not affected by the mass deposition and therefore that the mass loading effect exclusively dominates.

At this stage, two cases must be distinguished according to the type of mass deposition: either punctual or areal (also named distributed).

I.3.a.i) Punctual mass sensitivity

The punctual mass sensitivity corresponds to the measurement of punctual, spatially localized species like particles, droplets, bacteria, molecular aggregates, etc…

With the aim of determining the sensing attribute of a device, let us reformulate first eq.(II.43) to express the effective mass m_{EFF_P} :

$$m_{EFF_P} = \alpha_{1_P}\, m_{RES} = \frac{1}{4\pi^2}\frac{k_{EFF_P}}{f^2} \tag{II.44}$$

In this expression, the effective mass m_{EFF_P} corresponds to the equivalent mass of the whole resonator as if it were located in one single point. Depending on the position of this point, a specific corrective coefficient α_{1_P} must be applied. In the case of a cantilever, the α_{1_P} coefficient is equal to 0.25 for the free end point what means that the whole cantilever mass is equivalent to a four times smaller punctual mass exerted at its free end.

Considering an addition of mass upon the resonator restricted to a punctual location, the first derivative of the mass with respect to the frequency is calculated. It is necessary to derive the

effective mass m_{EFF}, and not the resonator mass m_{RES}, since the effective mass considered in eq.(II.44) can be directly seen as a true mass exerted at the point of mass deposition, in other words:

$$m_{EFF_FINAL} = \alpha_1 m_{RES} + \Delta m \tag{II.45}$$

where Δm is the punctual mass accretion. Hence, *S*, the punctual mass sensitivity, can be estimated in this way:

$$S = \left|\frac{\partial m_{EFF_P}}{\partial f}\right| = \left|\frac{\partial}{\partial f}\left(\frac{1}{4\pi^2}\frac{k_{EFF_P}}{f^2}\right)\right| \approx \frac{1}{2\pi^2}\frac{k_{EFF_P}}{f^3} = 2\frac{m_{EFF_P}}{f} \quad \left(g.Hz^{-1}\right) \tag{II.46}$$

This value of sensitivity is valid only around the initial resonance frequency and for small deviations. However, there is a more accurate way to estimate the corresponding amount of mass as a function of the frequency deviation. Considering that the effective mass before depositing is:

$m_{EFF_P_i} = \alpha_1 m_{RES} = \frac{1}{4\pi^2}\frac{k_{EFF_P}}{f_i^2}$, and after depositing is: $m_{EFF_P_f} = \alpha_1 m_{RES} + \Delta m = \frac{1}{4\pi^2}\frac{k_{EFF_P}}{f_f^{\,2}}$

so:

$$\Delta m = \frac{k_{EFF_P}}{4\pi^2}\left(\frac{1}{f_f^{\,2}} - \frac{1}{f_i^2}\right) \tag{II.47}$$

This method is more reliable as one directly bases on the initial and final value of the resonance frequency what is more confident than relying on an estimated mass sensitivity that is only valid around the unloaded resonance frequency value.

I.3.a.ii) Areal mass sensitivity

The determination of the areal mass sensitivity is required to quantify in terms of mass some resonance frequency shifts related to uniformly deposited masses, like when depositing layers of a material in an evaporation chamber. Let us reformulate eq.(II.43) to express the effective mass m_{EFF_A}:

$$m_{EFF_A} = \alpha_{1_A}\, m_{RES} = \frac{1}{4\pi^2}\frac{k_{EFF_A}}{f^2} \tag{II.48}$$

In this case, on the contrary to punctual deposition, the new value of the effective mass after uniform deposition is

$$m_{EFF_A} = \alpha_{1_A}\left(m_{RES} + \Delta m\right) \tag{II.49}$$

where $\Delta m = \rho_M\, A\, \Delta e = S_A\, A\, \Delta f$ (ρ_M is the deposited material density, *A* the resonator area on the side where the mass is deposited, Δe the deposited thickness, S_A the areal mass sensitivity and Δf the resulting frequency shift). Actually, the accreted mass must be corrected by α_{1_A} (areal effective mass coefficient) as it is spread all over the resonator area.

Considering a uniform addition of mass upon the resonator, the first derivative of the mass with respect to the frequency is calculated. From eq.(II.49), it is clear that the proper resonator

mass, and not the effective mass, must be derived. S_A, the areal mass sensitivity, can therefore be estimated in this way:

$$S_A = \frac{1}{A}\left|\frac{\partial m_{RES}}{\partial f}\right| = \frac{1}{A}\left|\frac{\partial}{\partial f}\left(\frac{1}{4\pi^2\alpha_{1_A}}\frac{k_{EFF_A}}{f^2}\right)\right| \approx \frac{1}{A}\frac{1}{2\pi^2\alpha_{1_A}}\frac{k_{EFF_A}}{f^3} = 2\frac{1}{A}\frac{m_{RES}}{f} \quad \left(g.Hz^{-1}.cm^{-2}\right) \quad \text{(II.50)}$$

This value of sensitivity is valid only around the initial resonance frequency and for small deviations. However, as previously said, there is another approach, more accurate. Considering that the effective mass before depositing is:

$m_{EFF_A_i} = \alpha_{1_A} m_{RES} = \frac{1}{4\pi^2}\frac{k_{EFF_A}}{f_i^2}$, and after depositing is: $m_{EFF_A_f} = \alpha_{1_A}\left(m_{RES} + \Delta m\right) = \frac{1}{4\pi^2}\frac{k_{EFF_A}}{f_f^{\,2}}$

this results in [14]:

$$\Delta m = \rho\, A\, \Delta e = \frac{k_{EFF_A}}{4\pi^2\alpha_{1_A}}\left(\frac{1}{f_f^{\,2}} - \frac{1}{f_i^2}\right) \quad \text{(II.51)}$$

I.3.b. Dynamic linear range

The linear range of the mass sensor is given at its lower limit by the frequency noise floor while its upper limit is reached when the effective spring constant k_{EFF} is modified (either by an additional stiffening caused by the accretion or by an adsorption induced surface-stress).

When depositing mass on top of the resonator, one can make the assumption that until a certain limit the resonator will still remain in its linear elastic mechanical regime, i.e. that k_{EFF} still remains constant. Hence, a change in S does not mean automatically that the resonator enters a mechanical nonlinear regime but rather simply than m_{EFF} and f_0 vary in eq.(II.46) or (II.50). Thus, a quasi-linear approach can be followed to predict the sensor response. Let us write the resonance frequency as a function of the deposited mass for a punctual (left) or distributed (right) mass loading:

$$f_{RES} = \frac{1}{2\pi}\sqrt{\frac{k_{EFF_P}}{m_{EFF_P} + m_{DEPOSITED_PUNCTUAL}}} \quad \text{and} \quad f_{RES} = \frac{1}{2\pi}\sqrt{\frac{k_{EFF_A}}{\alpha_{1_A}\left(m_{RES} + m_{DEPOSITED_AREAL}\right)}} \quad \text{(II.52)}$$

what can be re-written as:

$$f_{RES} = f_0\sqrt{\frac{m_{EFF_P}}{m_{EFF_P} + m_{DEPOSITED_PUNCTUAL}}} \quad \text{and} \quad f_{RES} = f_0\sqrt{\frac{\alpha_{1_A} m_{RES}}{\alpha_{1_A}\left(m_{RES} + m_{DEPOSITED_AREAL}\right)}} \quad \text{(II.53)}$$

what can be further simplified as:

$$f_{RES} = f_0\sqrt{\frac{1}{1 + \frac{m_{DEPOSITED_PUNCTUAL}}{m_{EFF_P}}}} \quad \text{and} \quad f_{RES} = f_0\sqrt{\frac{1}{1 + \frac{m_{DEPOSITED_AREAL}}{m_{RES}}}} \quad \text{(II.54)}$$

These two equations can help in predicting the resonance frequency decrease along the mass deposition. They remain valid only while the stiffness remains constant, what is true until the mass deposit is large enough so that it generates an additional stiffening of the structure or a surface stress.

II. Electrical response of electrostatically driven resonators

In chapter 1, different techniques have been mentioned to actuate and detect the mechanical resonance spectrum of nano/micromechanical devices. We have chosen an all electric actuation and detection scheme, concretely electrostatic actuation and capacitive detection. The advantages of this approach compared to other methods are detailed hereafter.

Optical characterization is an expanded and classical way to measure resonance frequencies as it offers a very high resolution in terms of spatial displacements (i.e. oscillation amplitudes). Yet, its implementation is not suitable here for several reasons.

In particular, issues related to the laser spot are problematic. The spot size, in general in the micron range, may be a limitation compared to nanometer scale resonator dimensions, and its alignment with the device may be another issue. Furthermore, AFM-based and interferometric optical techniques are limited to out-of-plane vibrations only. For measuring several devices at the same time, for example an array of resonators for multiple samples detection, several laser beams would be required and the resulting practical implementation is rather complex.

Magnetomotive detection is another approach to detect mechanical oscillations but it requires a heavy set-up under high magnetic fields (1-10 Tesla).

Piezoelectric and piezoresistive detection schemes are also possible but the capacitive technique provides a favorable trade-off between simplicity of implementation, displacement sensitivity and system portability. It does not require any material (unlike the piezoelectric approach) incompatible with a CMOS process. It also opens up possibilities of simultaneously operating multiple devices (arrays) without requiring heavy set-ups neither alignment.

The smartest realization of NEMS embedded in a capacitive detection scheme is a monolithic integration with CMOS circuitry. It makes possible "on-chip" signal processing (amplification and conditioning), additionally arrays of sensors can be operated while the overall system remains ultra-compact and light. The integration of NEMS on CMOS will be described in chapters 3, 4 and 5.

II.1. Transduction principle: capacitive detection with electrostatic actuation

In our approach, mechanical resonators are electrostatically actuated and a capacitive detection scheme converts mechanical oscillations into an electrical signal.

The global system is illustrated, taking the example of a cantilever, in Figure 8: it consists of a driver, mechanically fixed, and a cantilever placed in parallel very close to the driver. It can freely bend around the static position at a given oscillation frequency.

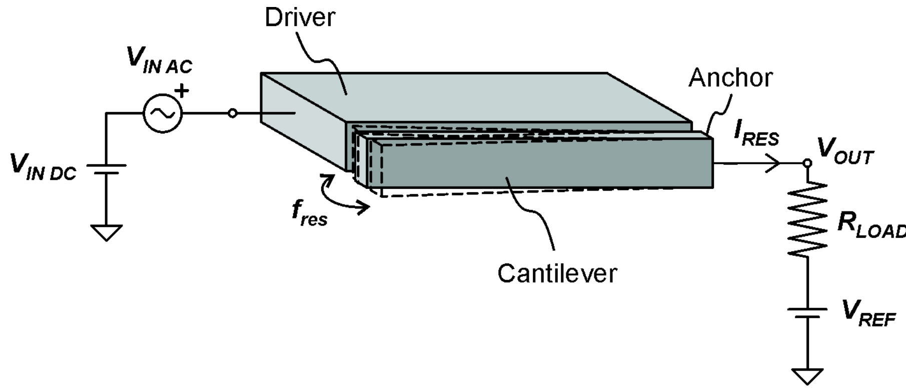

Figure 8. All electric actuation and detection scheme for a cantilever

The fixed driver is devoted to bias the required DC voltage $\left(V_{IN\,DC} - V_{REF}\right)$ (typically 1 V to 30 V) and to act as the input terminal for the alternate voltage stimulation $V_{IN\,AC}$ (typically -30 dBm to 0 dBm). On the other hand, the cantilever plays the role of the output terminal, allowing the readout of the resonator oscillation current I_{RES} (typically in the range of nA), subsequently converted into a voltage V_{OUT} by the load resistor R_{LOAD}. The resonance frequency depends on the resonator material, shape and dimensions as previously detailed.

The mechanical motion is translated into an electrical signal (subsequently collected and conditioned by a read-out device) through a capacitive transduction. In fact, the capacitive current generated by the two-electrodes system can be described as:

$$\begin{aligned} i_{RES}(t) &= \frac{dQ_{RES}}{dt} = C_{NEMS}\frac{d\left(V_{IN\,DC} - V_{REF} + V_{IN\,AC}\right)}{dt} + \left(V_{IN\,DC} - V_{REF} + V_{IN\,AC}\right)\frac{dC_{NEMS}}{dt} \\ &\approx C_0\frac{dV_{IN\,AC}}{dt} + \left(V_{IN\,DC} - V_{REF}\right)\frac{dc}{dt} \end{aligned} \quad \text{(II.55)}$$

where $C_{NEMS}(t) = C_0 + c(t)$, *Co* is the static component and *c* the time dependant one of the (here, in-plane) capacitor cantilever/air/electrode. It is assumed that $V_{IN\,DC} - V_{REF} \gg V_{IN\,AC}$.

Thus, the NEMS current can be understood as a sum of two contributions of current: (i) one arising from the static structure: $i_S = C_0\frac{dV_{IN\,AC}}{dt}$ and (ii) the other coming from the resonator mechanical motion $i_M = \left(V_{IN\,DC} - V_{REF}\right)\frac{dc}{dt}$. This latter component allows measuring the frequency response of the resonator.

II.2. Equivalent electrical modeling of a mechanical resonator

II.2.a. Global equivalent electrical scheme

Equation (II.55) describes an ideal case in which no parasitic capacitances affect the measurement. As a matter of fact, the total generated capacitive current is not only a sum of

motion and static components but also of a parasitic component, usually the most significant fraction of the total. In fact, this high parasitic component may even "hide" the motional current. For a more accurate prediction of the resonance signal level, the mechanical resonator is modeled in the following way:

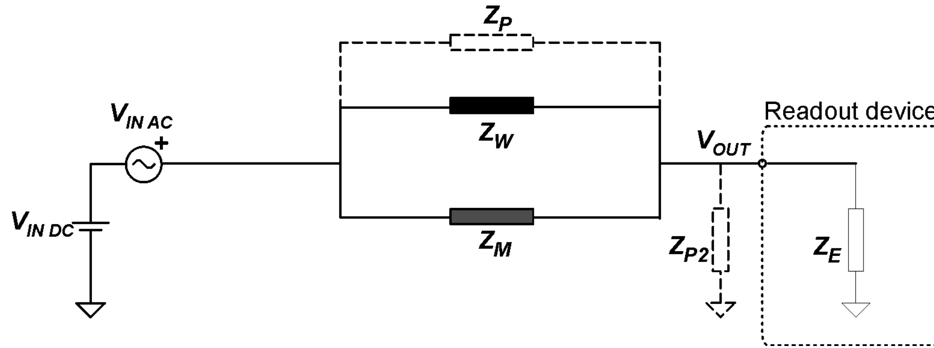

Figure 9. Actuation and detection electrical scheme including parasitic components

where Z_P is a parasitic impedance existing between input and output terminals, Z_W the impedance associated to the static capacitor, Z_M the impedance associated to the mechanical motion occurring around resonance, Z_{P2} the equivalent parasitic impedance at the output port and Z_E the input impedance of the readout device (a network analyzer in the case of discrete devices, a CMOS circuit in monolithic systems).

GENERAL BEHAVIOR

As a first remark, it should be stated that all over the work presented in this thesis, the resonators structural layer (either mono- or polycrystalline silicon) is always sufficiently doped with phosphorous (n-type) so that we consider it as a good conductor of negligible resistivity.

Z_P deeply depends upon the type of resonator and on its electrodes configuration. It can be approximated as:

$$\boldsymbol{Z_P} \approx \frac{1}{\boldsymbol{C_P}\,\omega} \tag{II.56}$$

where C_P is the parasitic stray capacitance and ω the angular frequency of operation.

In the case of in-plane vibrating cantilevers, this impedance corresponds to the capacitance related to the fringing electrostatic field and the resulting impedance is usually very high. For other types of resonators, in particular out-of-plane vibrating devices, it may be dramatically low because of a strong capacitive coupling between the underlying layer acting as input terminal and the resonator anchors (belonging to the structural layer, i.e. the output terminal). This will be detailed in section III.1.c.i). As a design rule, Z_P should be maximized (i.e. C_P reduced).

Z_W depends on the resonator geometry: it is associated to the static capacitance C_W of the resonator/air/input terminal capacitor:

$$\boldsymbol{Z_W} \approx \frac{1}{\boldsymbol{C_W}\,\omega} \approx \frac{\boldsymbol{d}}{\varepsilon_0 \boldsymbol{A}\,\omega} \tag{II.57}$$

where ε_0 is the vacuum dielectric constant, A the capacitor area, d the gap between resonator and input port, and ω the angular frequency of operation.

Z_M is the motional impedance of the resonator. The lower it is, the higher is the signal generated by the mechanical resonance. An important challenge to address is the implementation of a reliable model in order to be able to translate mechanical parameters such as k, m and D (refer to eq. (II.3)) into electrical equivalent parameters. Thus, the levels of electrical signal generated during mechanical resonance could be assessed.

Z_{P2} is related to parasitic capacitances located at the output terminal. In an experimental set-up for discrete devices, the total parasitic capacitance arises from the measurement instrumentation and is in the order of tens of pF (what corresponds to parasitic capacitances respectively of the wire bonding between chip and printed circuit board (PCB), of the PCB itself and of the coaxial cables).

In case of a monolithic integration, this capacitance is in the order of tens of fF (three orders of magnitude less) and corresponds to a parasitic physical capacitor related to the routing between the resonator output terminal and the CMOS circuit input. As a design rule, Z_{P2} should be maximized (i.e. C_{P2} reduced).

Z_E is the input impedance of the readout device. The network analyzer we use for device frequency characterization is configurable at either 50 Ω or 1 MΩ.

The resulting load resistance $\boldsymbol{R_{LOAD}}$ (see Figure 8) that converts the resonance current into $\boldsymbol{V_{OUT}}$ is given by:

$$\frac{1}{\boldsymbol{R_{LOAD}}} = \frac{1}{\boldsymbol{Z_{P2}}} + \frac{1}{\boldsymbol{Z_E}} \quad \Rightarrow \quad \boldsymbol{R_{LOAD}} = \frac{\boldsymbol{Z_{P2}}\,\boldsymbol{Z_E}}{\boldsymbol{Z_{P2}} + \boldsymbol{Z_E}} \tag{II.58}$$

Usually, C_{P2} is quite high what is equivalent to a low Z_{P2}. Yet, Z_{P2} is usually larger than 50 Ω and in this case, it is more favorable to set Z_E to 1 MΩ, what makes that Z_{P2} dominates and acts as load resistance (instead of 50 Ω).

II.2.b. RLC equivalent model of the motional impedance

This section presents a model that allows estimating the electrical behavior of a mechanical resonator. From a phenomenological point of view, a D, m, k [c.f. eq.(II.3)] mechanical oscillator is equivalent to a small signal electrical RLC oscillator [18-21]. A conversion scale factor is needed to transfer mechanical signals domain to an electrical signals domain. These issues are detailed hereafter.

II.2.b.i) Phenomenological approach of a RLC oscillator

The objective here is to determine the frequency response, and its key features, of two oscillators, pure RLC and RLC in parallel with C, by calculating their transfer function. Through the study of such classical electrical components, the electrical behavior of a mechanical resonator can be qualitatively predicted.

RESPONSE OF A SINGLE RLC BRANCH

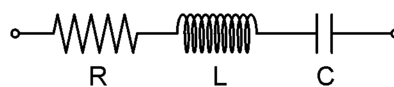

Figure 10. RLC branch

A single RLC branch provides a similar response than a pure mechanical resonator. The intrinsic mechanical response is accessible for instance via optical techniques, what is not the case of capacitive detection as it will subsequently explained. The impedance of the branch is:

$$Z_{RLC} = \frac{1}{jC\omega} + jL\omega + R \tag{II.59}$$

setting $s = j\omega = j2\pi f$, then: $Z_{RLC} = \frac{1}{jC\omega} + jL\omega + R = \frac{LCs^2 + RCs + 1}{Cs}$

The resonator current is given by: $i_{RLC} = \frac{V}{Z_{RLC}}$. Setting V=1, the frequency response is:

$$i_{RLC} = \frac{1}{Z_{RLC}} = \frac{Cs}{LCs^2 + RCs + 1} \tag{II.60}$$

while the resonance frequency is $f_{RES} = \frac{1}{2\pi}\frac{1}{\sqrt{LC}}$

In Figure 11 and Figure 12, typical magnitude and phase responses are plotted in different conditions: L and C are set to about 1 H and 10 fF (what results in f_{RES}≈1.5 MHz) while R is set to 5, 25 and 50 kΩ.

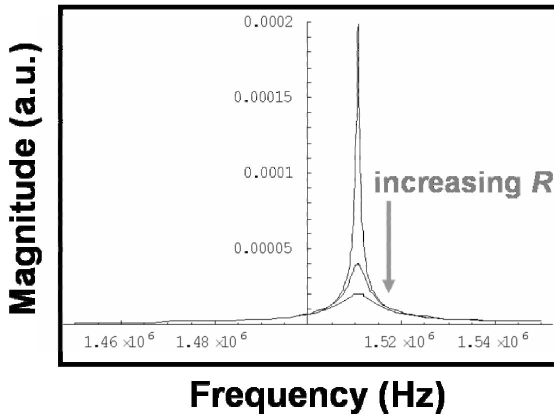

Figure 11. Typical magnitude response of a RLC branch

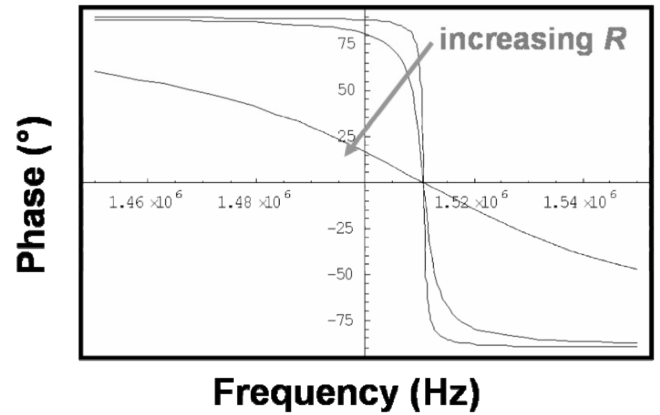

Figure 12. Typical phase response of a RLC branch

The key features here are the single peak in the magnitude spectrum and the 180° phase shift downwards around the resonance frequency.

At a given resonance frequency, the general trends are (i) increasing the inductance (i.e. decreasing the capacitance) tends to lower the peak magnitude and (ii) increasing R (maintaining L and C constant) tends to decrease the peak magnitude as well, worsens the peak quality factor and produces a less steep phase shift.

RESPONSE OF A DOUBLE BRANCH: RLC PARALLEL WITH C

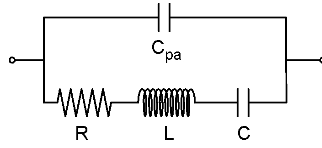

Figure 13. Double branch RLC in parallel with (parasitic) C_{PA}

This system is the most similar to the configurations of Figure 8 and Figure 9 whereby the mechanical resonator, equivalent to a RLC branch, is embedded in an electrical readout system based on a capacitive scheme. Let us see to what extent the unavoidable parallel capacitance (sum of parasitic and static contributions) modifies the NEMS frequency response.

The impedance of each branch is: $Z_{RLC} = \frac{1}{jC\omega} + jL\omega + R$ and $Z_{PA} = \frac{1}{jC_{PA}\omega}$

Setting $s = j\omega = j2\pi f$, then $Z_{eq} = \frac{1}{\frac{1}{Z_{PA}} + \frac{1}{Z_{RLC}}} = \frac{1}{C_{PA}s + \frac{1}{\frac{1}{jC\omega} + jL\omega + R}}$

$$\Rightarrow Z_{eq} = \frac{LCs^2 + RCs + 1}{LCC_{PA}s^3 + RCC_{PA}s^2 + (C + C_{PA})s} = \frac{1}{C_{PA}s} \frac{LCs^2 + RCs + 1}{\left(LCs^2 + RCs + \left(1 + \frac{C}{C_{PA}}\right)\right)}$$

Normalizing again V to 1, the frequency response of the resonator current is given by:

$$i_{RES} = \frac{1}{Z_{eq}} = C_{PA}s \frac{\left(LCs^2 + RCs + \left(1 + \frac{C}{C_{PA}}\right)\right)}{LCs^2 + RCs + 1} \quad \text{(II.61)}$$

In Figure 14 and Figure 15, typical magnitude and phase responses are plotted in different conditions: L and C are set to about 1 H and 10 fF (what results in f_{RES}≈1.5 MHz), C_{PA} is set to 1.5 pF while R is set to 2, 0.7 and 0.2 MΩ.

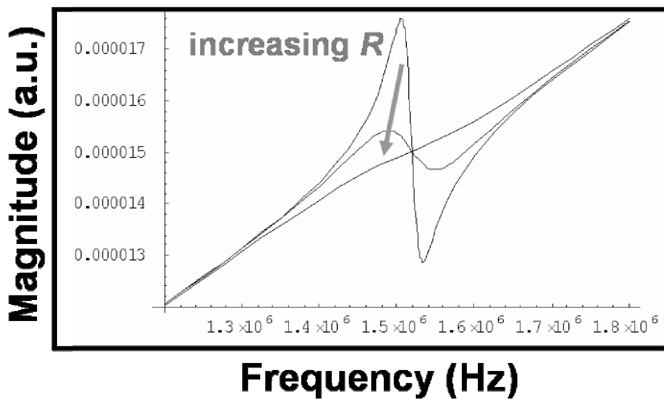

Figure 14. Typical magnitude response of a double branch RLC//C

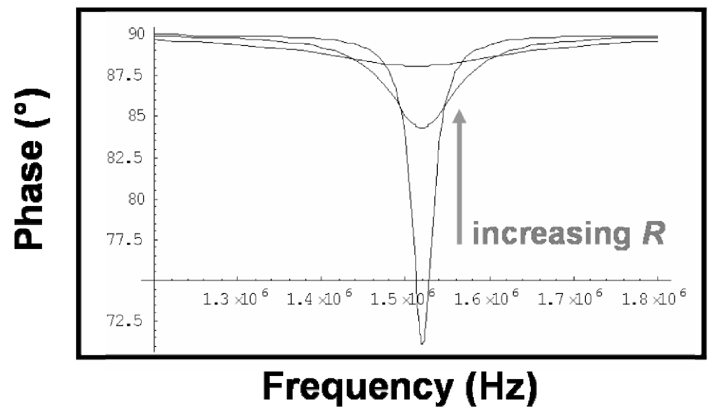

Figure 15. Typical phase response of a double branch RLC//C

Magnitude and phase spectra change radically compared to the behavior of a single RLC branch. Here, the magnitude response exhibits the proper resonance immediately followed by an anti-resonance peak. The background level is determined by C_{PA}. The phase response is no more stairs-like; the resonance provokes a phase shift down to lower values but comes back rapidly to the background value.

C_{PA} plays a key role: the higher it is the more pronounced is the magnitude anti-peak and the less pronounced is the phase peak.

II.2.b.ii) Parameters calculation

Now, the qualitative response of the system depicted in Figure 9 is known. Let us quantify Z_M the impedance illustrating the mechanical motion. Ideally, Z_M should be as low as possible in order to predominate against either Z_P or Z_W.

The mechanical resonator, characterized by its mechanical parameters k (resonator stiffness), m (resonator mass) and D (viscous damping coefficient related to the resonance quality factor Q, according to $D = \frac{\sqrt{km}}{Q} = \frac{m\omega}{Q}$), can be electrically modeled as a RLC branch. This electromechanical model assigns to each mechanical parameter an equivalent electrical value. We follow the approach from Mattila et al. [19]. Let us express the electrostatic force:

$$F_E = \frac{1}{2}\frac{\partial C}{\partial x}\left(V_{IN\,AC} + V_{IN\,DC}\right)^2 = \frac{1}{2}\frac{\partial C}{\partial x}\left(v_{AC}{}^2 \sin^2 \omega t + 2 v_{AC} V_{IN\,DC} \sin \omega t + V_{IN\,DC}{}^2\right) \text{ with } V_{IN\,AC} = v_{AC} \sin \omega t$$

actually, $\sin^2 \omega t = \frac{1 - \cos 2\omega t}{2}$, so

$$F_E = \frac{1}{2}\frac{\partial C}{\partial x}\left[\left(\frac{v_{AC}{}^2}{2} + V_{IN\,DC}{}^2\right) + 2 v_{AC} V_{IN\,DC} \sin \omega t - \frac{v_{AC}{}^2}{2}\cos 2\omega t\right] \quad \text{(II.62)}$$

The time-varying part of the capacitive driving force actuating the driven damped mass-spring system (eq.(II.8)) to the first order is:

$$F_E(t) = \frac{1}{2}\frac{\partial C}{\partial x}\left[2 v_{AC} V_{IN\,DC} \sin \omega t\right] = \frac{\partial C}{\partial x} V_{IN\,AC} V_{IN\,DC}$$

The global equation is: $$m\frac{d^2 x}{dt^2} + D\frac{dx}{dt} + kx = F_E(t) = \frac{\partial C}{\partial x} V_{IN\,AC} V_{IN\,DC}$$

that is to say: $$m\omega^2 x + D\omega x + kx = F_E(t) = \frac{\partial C}{\partial x} V_{IN\,AC} V_{IN\,DC} \quad \text{(II.63)}$$

As previously said (eq.(II.55)), the motional current i_M can be expressed as:

$$i_M \approx V_{IN\,DC}\frac{\partial C}{\partial t} = V_{IN\,DC}\frac{\partial C}{\partial x}\frac{\partial x}{\partial t} \Rightarrow V_{IN\,DC}\frac{\partial C}{\partial x} = \frac{i_M}{\dot{x}} = \frac{i_M}{\omega x} \quad \text{(II.64)}$$

Inserting (eq.(II.64)) into (eq.(II.63)), we obtain $m\omega^2 x + D\omega x + kx = \frac{i_M}{\omega x} V_{IN\,AC}$ and rewrite it as:

$$V_{IN\,AC} = \frac{m\,\omega^3 x^2}{i_M} + \frac{D\,\omega^2 x^2}{i_M} + \frac{k\,\omega\,x^2}{i_M} \tag{II.65}$$

On another part, basing on eq.(II.59),

$$V_{IN\,AC} = jL_M \omega i_M + R_M\, i_M + \frac{i_M}{jC_M \omega} \tag{II.66}$$

Identifying the complex modulus of the left terms of eq.(II.65) and (II.66),

$$L_M \omega\, i_M = \frac{m\omega^3 x^2}{i_M} \Rightarrow L_M = m\left[\frac{\omega^2 x^2}{i_M{}^2}\right] = \frac{m}{\eta^2} \tag{II.67}$$

we define η the electromechanical coupling coefficient that puts in relation electrical current and mechanical transducer velocity:

$$\eta = \frac{i_M}{\omega x} = \frac{i_M}{v(t)} = V_{IN\,DC}\frac{\partial C}{\partial x} \tag{II.68}$$

where $v(t)$ is the mechanical velocity

For small displacements, $\eta \approx \frac{\varepsilon_0 A}{d^2} V_{IN\,DC}$ where ε_0 is the vacuum dielectric constant, d the gap between resonator and input port, and A the capacitor area.

Identifying the two other terms of eq (II.65) and (II.66), it results in:

$$R_M = \frac{D}{\eta^2} = \frac{\sqrt{k\,m}}{Q\eta^2} = \frac{1}{Q}\sqrt{\frac{L_M}{C_M}} \qquad C_M = \frac{\eta^2}{k} \qquad L_M = \frac{m}{\eta^2} \tag{II.69}$$

Note that the resonance frequency of the electrical RLC branch is equal to the mechanical resonance:

$$f_{RES} = \frac{1}{2\pi\sqrt{L_M C_M}} = \frac{1}{2\pi}\sqrt{\frac{k}{\eta^2}\frac{\eta^2}{m}} = \frac{1}{2\pi}\sqrt{\frac{k}{m}} \tag{II.70}$$

Around resonance, C_M and L_M cancel each other and the branch becomes equivalent to a simple resistance whose value is R_M.

II.2.c. Global response

A general expression of the total capacitive current I_{MEMS} generated around resonance frequency is:

$$I_{MEMS}(t) = \frac{V_{IN\,AC}}{Z_{TOT}} = \sum i = i_P + i_W + i_M = \approx V_{IN\,AC}\left(C_P\omega + C_W\omega + \frac{1}{R_M}\right) \quad \text{(II.71)}$$

where i_P, i_W and i_M are the currents respectively associated to Z_P (i.e. C_P), Z_W (i.e. C_W) and R_M. $V_{IN\,AC}$ is the AC excitation voltage.

We define a figure of merit (*FM*),calculated at the resonance frequency, that points up the trend to generate a high resonance current compared to the currents arising from parasitic and static capacitances:

$$FM = 100\frac{i_M}{i_P + i_W} \quad in\,\% \quad \text{(II.72)}$$

Efforts on resonator design and readout configuration should focus on increasing *FM*.

So, computing eq.(II.71) with eq.(II.72),

$$FM = 100\frac{i_M}{i_P + i_W} = 100\frac{v_{AC}}{R_M}\frac{1}{v_{AC}\,\omega_0(C_P + C_W)} = 100\frac{Q\eta^2}{\sqrt{km}}\sqrt{\frac{m}{k}}\frac{1}{(C_P + C_W)} = 100\frac{Q\eta^2}{k(C_P + C_W)}$$

Inserting eq.(II.68) into the previous expression, we obtain the general formula:

$$FM = 100\frac{Q\varepsilon_0^{\,2} A^2 V_{IN\,DC}^{\;\;2}}{d^4(C_P + C_W)}\frac{1}{k} \quad in\% \quad \text{(II.73)}$$

where Q is the resonance quality factor, ε_0 is the vacuum dielectric constant, A is the resonator / gate electrode capacitor area and d the capacitor gap (assuming d is much larger than the resonator displacement). $V_{IN\,DC}$ is the applied DC voltage (assuming $V_{IN\,DC} >> V_{IN\,AC}$), and k the spring constant of the considered resonator.

II.3. Response to electrostatic actuation

This section is focused on the impact of electrostatic actuation on either the static or dynamic mechanical response of the resonator.

II.3.a. Deflection and pull-in voltage related to electrostatic force

Electrostatic actuation results in an attractive force that tends to bend the resonator towards the excitation electrode. It is of interest to quantify this deflection as it gives indications on the sensitivity of the displacement transducing scheme and allows predicting the pull-in voltage in order to prevent collapse and irreversible stiction of the resonator on its driving electrode.

In order to estimate the deflection, we equal the restoring spring force and the electrostatic force, neglecting air damping:

$$\left|F_e\right| = \left|F_k\right| \Rightarrow k\,x = \frac{1}{2}\frac{\partial C}{\partial x}V^2 \text{ with } V = V_{IN\,DC} + v_{AC}\sin\omega t$$

The electrostatic force involves time-constant and time-varying parts [see eq.(II.62)]:

$$F_E\left(\omega t\right) = \frac{1}{2}\frac{\partial C}{\partial x}\left[\left(\frac{{v_{AC}}^2}{2} + {V_{IN\,DC}}^2\right) + 2v_{AC}V_{IN\,DC}\sin\omega t - \frac{{v_{AC}}^2}{2}\cos 2\omega t\right] \quad \text{(II.74)}$$

Let us separate the two cases of static and dynamic deflection.

For the determination of the static deflection, the equation to solve is (assuming $V_{IN\,DC} >> v_{IN\,AC}$):

$$k\,x = \left|\frac{1}{2}\left(\frac{{v_{ac}}^2}{2} + {V_{dc}}^2\right)\varepsilon_0 A\frac{\partial}{\partial x}\left(\frac{1}{d-x}\right)\right| \Rightarrow x\left(d-x\right)^2 = \frac{\varepsilon_0 A}{2k}V_{IN\,DC}^2 \quad \text{(II.75)}$$

It comes that stable equilibrium positions only exist in the domain $0 < x < \frac{d}{3}$.

Let us introduce now the useful notion of pull-in voltage. Above this voltage, the electrostatic force is always greater than the spring force and the resonator is pulled towards the fixed electrode. The pull-in voltage is calculated at the limit $d/3$ of the stable domain:

$$V_{PI} = \sqrt{\frac{8k\,d^3}{27\varepsilon_0 A}} \quad \text{(II.76)}$$

In Table II - 5, the expression of the pull-in voltage is reported for two devices:

Device	k (N/m)	A (m²)	V_{PI} (V)
Cantilever In-plane flexion	$\frac{2}{3}\frac{E\,b^3\,h}{l^3}$	$h\,l$	$\sqrt{\frac{16\,E}{81\,\varepsilon_0}\frac{b^{3/2}\,d^{3/2}}{l^2}}$
Quad-beam Out-of-plane flexion	$\lambda_{QB}\frac{E\,h^3\,b}{l^3}$	L_1^2	$\sqrt{\frac{8\,\lambda_{QB}\,E}{27\,\varepsilon_0}\frac{h^{3/2}\,b^{1/2}\,d^{3/2}}{l^{3/2}\,L_1}}$

Table II - 5. Pull-in voltage formula for specific resonator designs

where λ_{QB} is a fitting factor in order to take into account deviations from the experimental resonance frequency. The effective factor of the cantilever spring constant (see α_2, section I.2.b.i)) is set to 2/3 since the electrostatic force is uniformly applied.

Around the static bending given by eq.(II.75), an additional periodic deflection is driven by the time-varying part of the electrostatic force. Neglecting the air damping, the oscillation amplitude x can be calculated as:

$$k\,x = \left|\frac{1}{2}2v_{AC}\,V_{IN\,DC}\varepsilon_0\,A\frac{\partial}{\partial x}\left(\frac{1}{d-x}\right)\right| \Rightarrow x\left(d-x\right)^2 = \frac{\varepsilon_0 A}{k}v_{AC}\,V_{IN\,DC} \qquad \text{(II.77)}$$

At large amplitudes, the resonator enters a mechanical nonlinear regime with hysteresis. In this regime, the dependence of the amplitude of vibration upon the axial force has to be taken into account, resulting in a non-linear term in eq.(II.3). The threshold amplitude, named critical amplitude [5, 22, 23] is given by:

$$x_c = \frac{\sqrt{2}\,b}{\left[\beta_n Q\left(1-\nu^2\right)\right]^{\frac{1}{2}}} \qquad \text{(II.78)}$$

where b is the resonator dimension in the direction of vibration, β_n is a coefficient depending on the mode and on the resonator shape, and υ is the Poisson's ratio of the structural material (for silicon: υ=0.28).

β_n depends on the structure and on the operated mode n. It is given by [23]:

$$\beta_n = \frac{3}{w_{n,MAX}^2(x)}\frac{\int_0^l\left(\frac{dw_n(x)}{dx}\right)^4 dx}{\int_0^l\left(\frac{d^2 w_n(x)}{dx^2}\right)^2 dx} \qquad \text{(II.79)}$$

where $w_n(x)$ is the approximate shape function of the nth mode and $w_{n,MAX}$ its maximum (see part I for the corresponding expressions of $w_n(x)$). For a cantilever beam vibrating in its fundamental mode, β_n =1.58; for a bridge β_n = 0.528 for the fundamental (flexural) mode.

In chapter 5, vibration amplitudes will be calculated when analyzing experimental results obtained on resonators that have been fabricated.

II.3.b. Spring-softening effect

To what extent electrostatic actuation influences the mechanical resonance frequency is an important issue. It has been experimentally observed, for example on cantilevers that an increasing applied voltage decreases the resonance frequency: this phenomenon arises from the so-called "spring-softening" effect [24, 25]. Hereafter, we propose an analytical explanation providing formulas of two specific mechanical structures. Let us consider the equation of the mass-spring system:

$$m\frac{d^2x}{dt^2} = F_{SP} = \frac{\partial F_{SP}}{\partial x}x = -kx \text{ leading to } f_o = \frac{1}{2\pi}\sqrt{\frac{k}{m}} \text{ (natural resonance frequency)}$$

If an electrostatic force is applied, then

$$m\frac{d^2x}{dt^2} = F_{SP} + F_E = \left(\frac{\partial F_{SP}}{\partial x} + \frac{\partial F_E}{\partial x}\right)x \equiv \left(-k + k_E\right)x$$

leading to $f' = \frac{1}{2\pi}\sqrt{\frac{k-k_E}{m}}$ (modified resonance frequency) with $k_E = \frac{\partial F_E}{\partial x}$

then, $f' = f_o\sqrt{1-\frac{k_E}{k}}$

At this stage, we use a Taylor development (since $k_E << k$) to obtain the relation between f' and f_0:

$$f' = f_o\left(1-\frac{k_E}{2k}\right) \tag{II.80}$$

The spring-softening effect depending on what point of view it is considered may represent either a drawback or an advantage. It tends to decrease the mass sensitivity according to eq.(II.46) ($2\,m/f$) but it makes the device more controllable as its resonance frequency is tunable, what may be interesting in particular to circumvent process-induced variations of dimensions.

RESONANCE FREQUENCY REDUCTION FOR AN IN-PLANE VIBRATING CANTILEVER

In this configuration, $F_E = -\frac{\varepsilon_0\, l\, h}{2(d-x)^2}V_{IN\,DC}{}^2$ assuming $V_{IN\,DC} >> V_{IN\,AC}$. Deriving F_E, we detail eq.(II.80) assuming $d >> x$ (x is the vibration amplitude):

$$f' = f_o\left(1-\frac{\varepsilon_0\, l\, h}{d^3}V_{IN\,DC}{}^2\frac{1}{2k}\right) \text{ and } k_{LATERAL} = \alpha_2\frac{E\,h\,b^3}{l^3}$$

where l, b and h are respectively the cantilever length, width and thickness. The electrostatic force is uniformly applied on the cantilever, consequently $\alpha_2 = \frac{2}{3}$. ($\alpha_2 = \frac{1}{4}$ is widely spread but is actually restricted to punctual force applied at the free end).

The detailed expression becomes:

$$f' = f_o\left(1 - \frac{3\varepsilon_0 l^4}{4Eb^3d^3}V_{IN\,DC}^{\;2}\right) = f_o\left(1 - KV_{IN\,DC}^{\;2}\right) \text{ with } K = \frac{3\varepsilon_0 l^4}{4Eb^3d^3} \tag{II.81}$$

where K stands as the electromechanical coupling factor.

RESONANCE FREQUENCY REDUCTION FOR AN OUT-OF-PLANE VIBRATING QUAD-BEAM

In this configuration, $Fe = -\frac{\varepsilon_0 L_1^{\;2}}{2(d-z)^2}V_{DC}^{\;2}$ assuming $V_{IN\,DC} >> V_{IN\,AC}$. Deriving F_e, we detail eq.(II.80) assuming $d >> z$ (z is the vibration amplitude):

$$f' = f_o\left(1 - \frac{\varepsilon_0 L_1^{\;2}}{d^3}V_{IN\,DC}^{\;2}\frac{1}{2k}\right) \text{ and } k = \lambda_{QB}\frac{Ebh^3}{l^3}$$

where L_1, l, b and h are respectively the central plate width, the beams length, width and the common thickness. To maintain a simple expression for the spring constant, we introduce λ_{QB}, an empirical factor extracted to fit with experimental values. We need to proceed with such an approximation since the effect of the underetching of the anchors, previously cited, drastically complicates the analytical formula. Typically, λ_{QB} is the range 1 – 4.

$$f' = f_o\left(1 - \frac{\varepsilon_0 L_1^{\;2} l^3}{2\lambda_{QB}Ebh^3d^3}V_{IN\,DC}^{\;2}\right) \tag{II.82}$$

GENERAL COMMENT ON HOW TO LESSEN SPRING-SOFTENING EFFECT

Looking at the expanded expression of the electrostatic force (eq.(II.74)), one can observe that both time-varying terms do not oscillate at the same frequency: the first term oscillates at the frequency ω of the driving signal and the second one at 2ω twice the driving frequency.

On the contrary to the term oscillating at ω, the second term depends exclusively on $V_{IN\,AC}$ and not on $V_{IN\,DC}$. Therefore, we might expect a less pronounced spring-softening effect as the alternate voltage magnitude is generally much weaker than the DC one. However, it must be stated that without DC voltage, the AC voltage must be much increased to excite enough the system. This tends to operate the resonator in its non-linear regime, what may be unwanted.

II.3.c. Generalization

In the literature, resonance frequency tuning with electrostatic actuation has been demonstrated [26, 27] both upward and downward. Very few authors have clearly explained the origins of both opposite trends in electrostatic nano/microresonators. Let us call the influence of the driving electrostatic signal on the resonance frequency as amplitude-frequency (A-f) effect.

Some authors have recently developed relatively general theoretical and qualitative models but focusing only on doubly clamped resonators (bridges). Basing on their statements, we propose a general qualitative explanation of both phenomena applicable to every resonator.

The opportunity to tune the resonance frequency is particularly interesting for applications oriented to telecommunications systems and more primarily to compensate unavoidable variations of devices dimensions related to technological process fluctuations. Various reversible frequency tuning mechanisms have been explored in the past: in particular stiffness variation with thermal stress [28] and electrostatic tuning [29, 30].

In quartz [31] devices and Si NEMS, the nonlinear *A-f* effect limits the maximum sustainable drive amplitude and hence the maximum SNR that can be achieved [32, 33]. Beyond the sustainable drive current, the resonant amplitude and phase response exhibit Duffing bifurcation instabilities [33, 34], as well as excess phase noise induced by amplitude noise [35]. It is of interest to determine the optimal bias condition in order to maximize the response.

These tuning behaviors are characteristic of nonlinearities. Actually, they come from the nonlinearities of two counterbalancing forces: spring force and electrostatic force resulting respectively in mechanical stiffening and electrical softening.

The most general rule than we can establish is:

- when the frequency is tuned upwards with increasing voltage (either AC or DC or a sum of both), it means that elastic frequency tuning dominates. In other words, the effect of the capacitive forces is weaker than the mechanical stiffening *A-f* effect: the electrostatic attraction stretches the resonator and causes an additional tensile axial force that tends to increase the resonance frequency (like in a guitar string, this effect is also named 'hard-spring' effect [23]).
- when the frequency is tuned downwards with increasing voltage, capacitive frequency tuning dominates: the softening *A-f* effect related to the capacitive forces [see eq.(II.80)] is stronger than the mechanical stiffening *A-f* effect.

Based on these two statements, each resonator will exhibit a specific behavior depending on its configuration (direction of the driving electrostatic field with respect to the direction of vibration [27]), and initial state (for example, stress in resonators may impose a bending towards or opposite the electrode and favor one type of behavior or another). This behavior can be either monotonous or with several states [26]. What can be added is that for optimal driving polarization, the interaction of the opposing mechanical stiffening and electrical softening leads to an increase in the amplitude while the frequency remains stationary. Agarwal [26] reports that the *A-f* coefficient in Si NEMS/MEMS is several orders of magnitude larger than quartz crystals what may be interesting for tuning.